Analysis report on the $ep \to ep\pi^+\pi^-$ reaction in the CLAS detector with a 5.754 GeV beam for $2.0 < Q^2 < 5.0\ \mathrm{GeV}^2$ and $1.4 < W < 2.0\ \mathrm{GeV}$

E. Isupov, V. Burkert, K. Hicks, V. Mokeev

July 28, 2016

Contents

List of Figures

Chapter 1

Data selection

In this note we report analysis of the CLAS data collected during e1-6 run period with electron beam energy of $E_b = 5.754$ GeV.

We extended considerably available information([13], [14]) on unpolarized cross sections of this exclusive channel. For the first time nine differential cross-section $\gamma_v p \to \pi^- \pi^+ p$ exclusive channel were measured at highest photon virtualities ever achieved in the studies of this exclusive channel from 2.0 GeV^2 to 5.0 GeV^2. They consist of:

- 3 invariant mass distributions for various pairs of the final particles $\frac{d\sigma}{dM_{\pi^-\pi^+}}$, $\frac{d\sigma}{dM_{\pi^+p}}$, $\frac{d\sigma}{dM_{\pi^-p}}$;
- 3 angular distributions over CM-emission angles for the final π^-, π^+ and protons;
- 3 angular distributions over the angles between two planes: first is composed by the initial photon and one of the final hadron 3-momenta, second plane contains 3-momenta of two other final hadrons for 3 various choices amongst the final particle pairs. Detailed description of 3-body kinematics is in the section 2.1.

Overall 9 single-differential cross-sections were measured in each (W & Q^2) bin. The data were collected at invariant masses of the final hadronic system from 1.4 to 2.0 GeV and at photon virtualities from 2.0 to 5.0 GeV^2 with 0.025 GeV step over W and variable bin size over Q^2. All differential and fully integrated cross-sections can be seen via the link
`https://www.jlab.org/Hall-B/secure/e1/isupov/final/section1.html`

1.0.1 Run Information

The data was collected from October 2001 until January 2002 (about 1000 hours of beam time) during e1-6 run. The beam energy was 5.754 GeV. The target was liquid Hydrogen, the length of the target 5 cm. The Torus magnetic field was 3375 A and mini-torus 6000 A. With an acquisition rate of 1.5 kHz, beam current about 7nA, and dead time of about 5%, 1.25 billions events were recorded, corresponding to run numbers from 30540 to 31484. The trigger was set on the threshold of CC(20 mV) and EC(75 for the inner part, 175 for the total). We used hbook files made by the program nt10maker from cooked BOS files. The files are available in the directory (/mss/clas/e1-6a/production/pass1/v1/pawnt/).

1.1 Selection of the $ep \rightarrow ep\pi^+\pi^-$ events

1.1.1 Selection of electron tracks

After cooking, the "first track" is assigned to the particle most likely to have triggered the event. We apply "$status > 0$" cut which rejects tracks which pass the Hit Based Tracking (HBT) but fail the Time Best Tracking (TBT) tests. Also we apply Z vertex cut to eliminate the electrons originating from the window located 2 cm downstream the target cell. The calculation of Z_{vtx} includes a correction due to misalignment of the target along the CLAS axis: during the experiment, the beam was centered, but the distribution of X_{vtx} and Y_{vtx} for the above mentioned window lead to an offset of the target of $X_{tgt} = 0.090cm$ and $Y_{tgt} = -0.345cm$. The Z_{vtx} distributions after this correction for 6 sectors with the cut $-8cm < Z_{vtx} < -0.8cm$ applied is shown(Fig. 1.1). Note that the target center is not exactly at the nominal -4 cm location.

A cut on the energy of the scattered electron is made due to calorimeter trigger. This cut was established in [1]. According to these studies $EEC(MeV) = 214 + 2.47 * EC_{thresh}(mV)$, where $EC_{thresh} = 175mV$, so $EEC(MeV) = 646MeV$, and due to fluctuations of the amplitude of the triggering signal, we apply 700 MeV cut.

If an electron enters the electromagnetic calorimeter too close to one of its edges (less than about 10 cm), the electromagnetic shower is not fully contained in the detector and the deposited energy is no longer related to the particle energy. The fiducial cuts are applied on local coordinates U_{EC}, V_{EC} and W_{EC}, calculated from the global coordinates X_{EC} and Y_{EC}. The following cuts are applied : $U_{EC} \geq 40$, $V_{EC} \leq 360$ and $W_{EC} \leq 390$. The distributions U_{EC}, V_{EC} and W_{EC} with applied cuts are shown on Fig. 1.2.

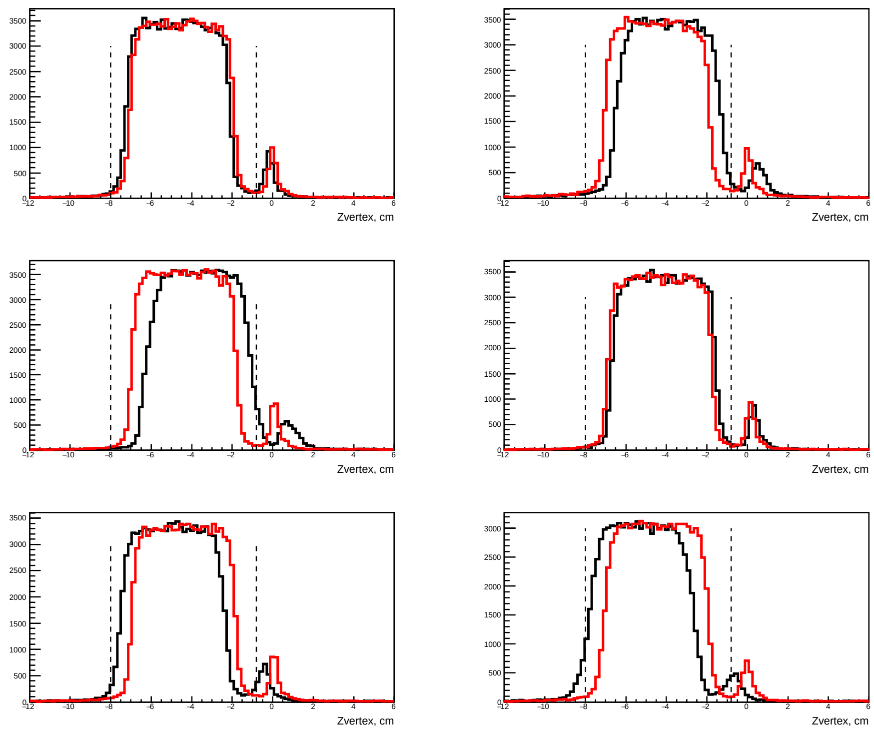

Figure 1.1: The Z_{vtx} distributions for electrons for 6 sectors with the cut $-8cm < Z_{vtx} < -0.8cm$. Black - not corrected data. Red - with correction due to offset in X_{tgt} and Y_{tgt}

1.1.2 e^-/π^- separation

The first tracks, as determined at cooking, contains pions misidentified as electrons. To reject these events we use calorimeter cuts.

Minimum ionizing pions are expected to lose 26 MeV of energy in 15 cm of scintillating material of the inner part of the calorimeter. A cut $E_{in} > 60MeV$ eliminates most of these pions (Fig. 1.3).

A more precise selection of electrons comes from the expected proportionality of deposited energy in the calorimeter and their momentum. Because of the sampling fraction, one expects $E_{TOT}/p \approx 0.29$.

The Fig. 1.4 shows that this ratio depends slightly on the momentum p.

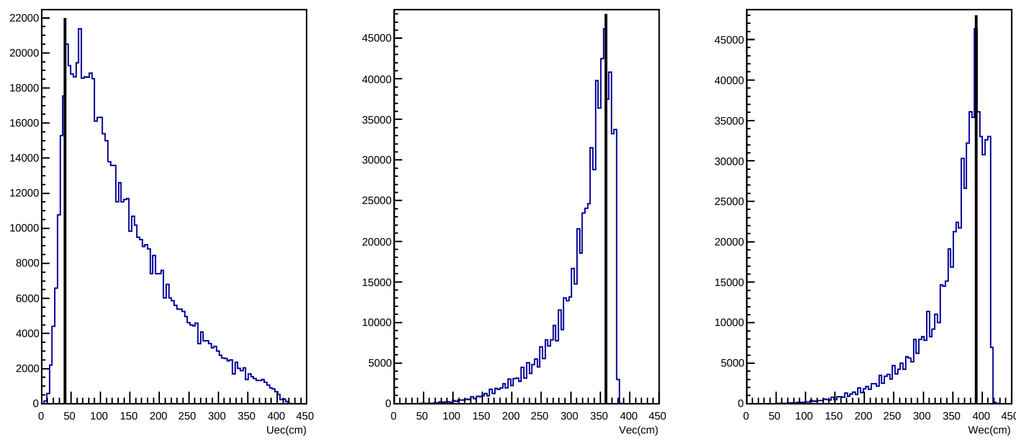

Figure 1.2: The distributions U_{EC}, V_{EC} and W_{EC} and applied fiducial EC cuts

We use the following cut:

$$\mid \frac{E^*_{TOT}}{p} - \mu \mid \leq 2.5 \times \sigma \tag{1.1}$$

where

- $E^*_{TOT} = MAX(E_{TOT}, E_{IN} + E_{OUT})$
- $\mu = 0.25069 + 0.042727 \times p - 0.01132 \times p^2 + 0.0010782 \times p^3$
- $\sigma^2 = (0.0303/\sqrt{p})^2 + 0.007761^2$

The use of E^*_{TOT} is meant to avoid a confusion between an electron and a nearby radiated photon. In case of two close hits in the EC, it is possible that the track identification at cooking assigns the E^*_{TOT} of the photon to the pair E^*_{IN}, E^*_{OUT} of the electron, or vice-versa. Since the electron is more likely to deposit higher energy, the definition E^*_{TOT} remedies that problem.

We also apply CC matching cuts[3] to suppress background PMT noise.

1.1.3 Electron fiducial cuts

The detector is composed of 6 independent sectors delimited by coils. There are some regions where the particle reconstruction is either incomplete or

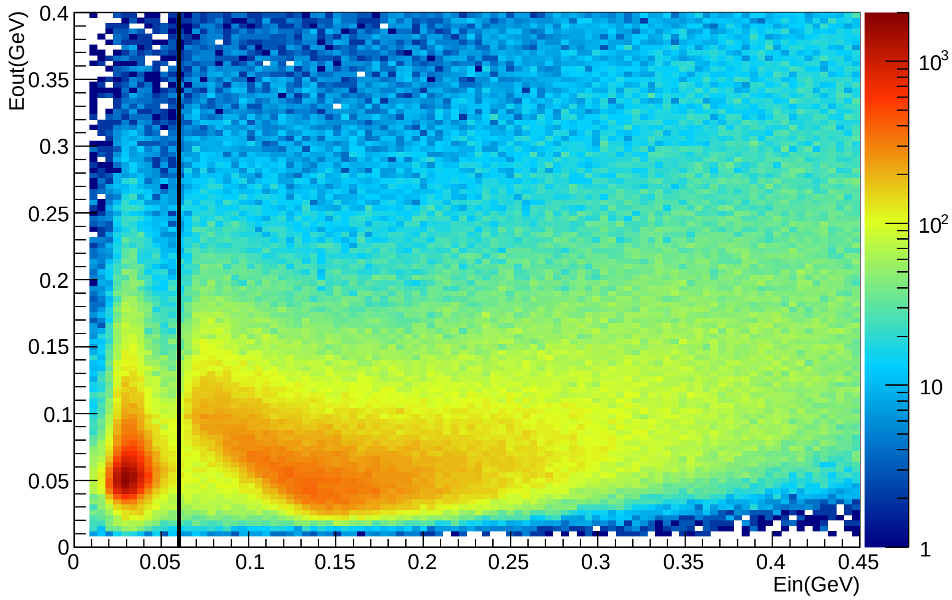

Figure 1.3: E_{out} vs E_{in}. The pions can be seen on the left. The right spot corresponds to electrons

poorly determined. The fiducial cuts throw out the particles which go into these parts of the detector, in order to increase the quality of the data. Using the data, we can detect these low detector efficiency regions where the efficiency is not uniform. These cuts are applied on the angle ϕ, and depend on the polar angle θ and the momentum p. A CLAS standard parametrization is applied

$$\theta \geq \theta_{cut}, \theta_{cut} = C_1 + \frac{C_2}{(p + p_{shift})} \tag{1.2}$$

$$|\phi_S| \leq C_4 \times sin(\theta - \theta_{cut})^{C_3 p^{\alpha}}$$

where ϕ_S is the azimuthal angle with respect to the center of the corresponding sector. For the $\mathrm{e}1-6$ run, the following values of parameters were determined[4]: $C_1 = 12^o$, $C_2 = 18.5^o/GeV$, $C_3 = 0.25GeV^{-\alpha}$, $C_4 = 25^o$, $\alpha = 0.416667$ and $p_{shift} = 0.14GeV$.

We also found that there are regions of depletion in the θ vs p distributions. This may be the signs of malfunctioning wires in the Drift Chamber

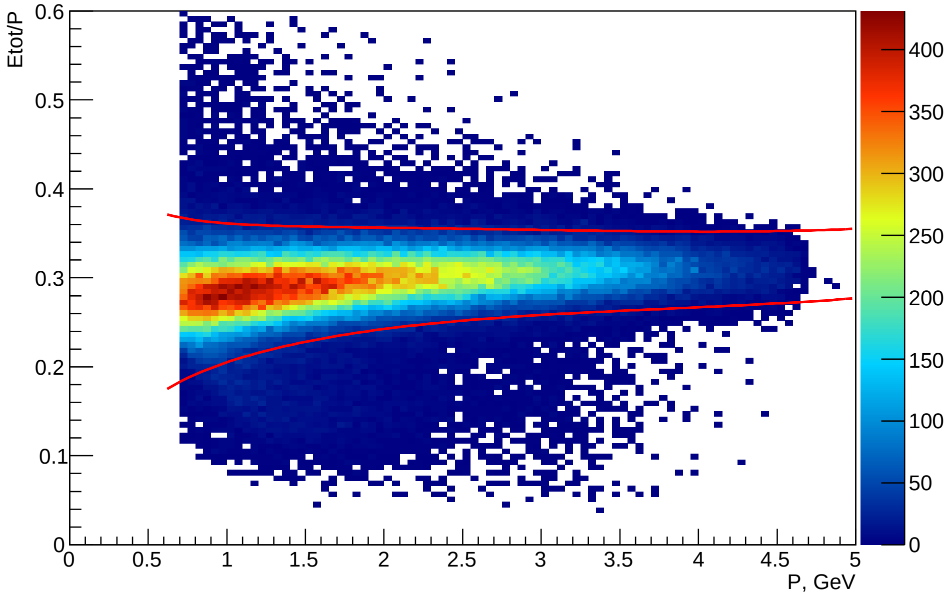

Figure 1.4: Sampling fraction(E_{TOT}/p)

system. We apply additional cuts to reject these regions. An example of such a distribution for sector 5 and corresponding cuts are shown on the Fig. 1.6.

1.1.4 Momentum corrections

For the momentum corrections of the electron and positive pion we use the procedure developed by Kijun Park, details can be found in [5].The distributions of elastic peak and missing mass of the neutron in reaction $ep \to en\pi^+$ before corrections are shown on the Figures 1.7, 1.8. The result of momentum corrections on these distributions can be seen on the Figures 1.9 and 1.10.

1.2 Hadrons identification

We select only those tracks where an electron was identified as mentioned in section 1.1.1.

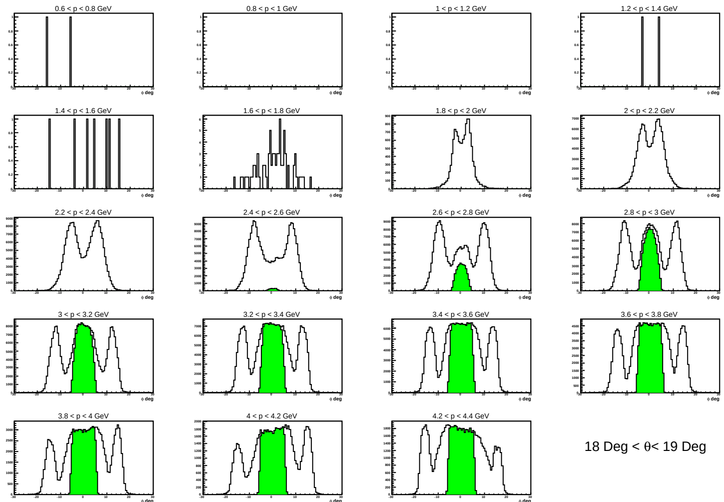

Figure 1.5: Example of the electron fiducial cut. The ϕ distribution for slices in θ and momentum. The green area is retained.

1.2.1 Identification cuts

For hadron identification we use a $\Delta\beta$ vs momentum cut. The cut uses information from time-of-flight and drift chambers. We can take β from the SC and also we can calculate β using momentum from the DC, but we must assign a specific mass in the latter case. We construct the difference between these two β.

$$\Delta\beta(m) = \beta_{meas} - \beta_{calc}(m) = l/ct - p/\sqrt{p^2 + m^2}$$

Figure 1.11 shows $\Delta\beta(m)$ as a function for positively charged hadrons. Protons appear as a horizontal stripe at $\Delta\beta(m_p) = 0$. The width of this proton distribution was found to be nearly independent of p(which is the main reason to use this cut rather on other equivalent quantities). The protons are then selected through $|\Delta\beta(m_p)| < 0.05\,(2\sigma)$.

To identify positive pions, we use $\Delta\beta(m_\pi)$ vs p as shown in the Figure 1.12. This leads to a pion selection cut $|\Delta\beta(m_\pi)| < 0.045(2\sigma)$.

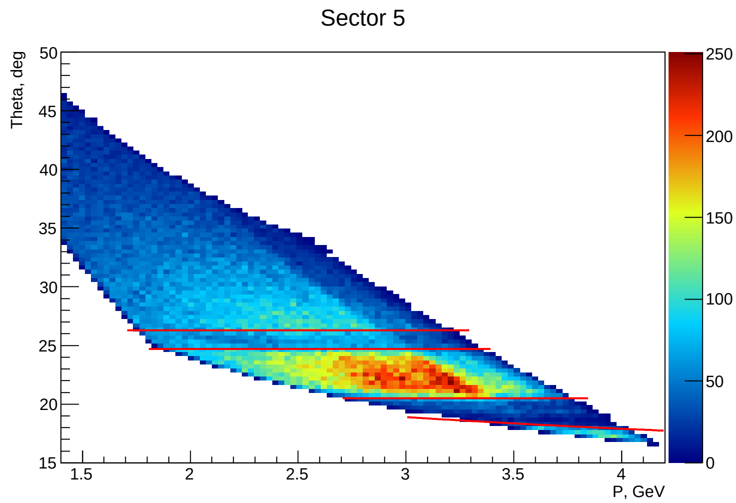

Figure 1.6: Electrons: θ vs p distribution for sector 5 with additional fiducial cuts

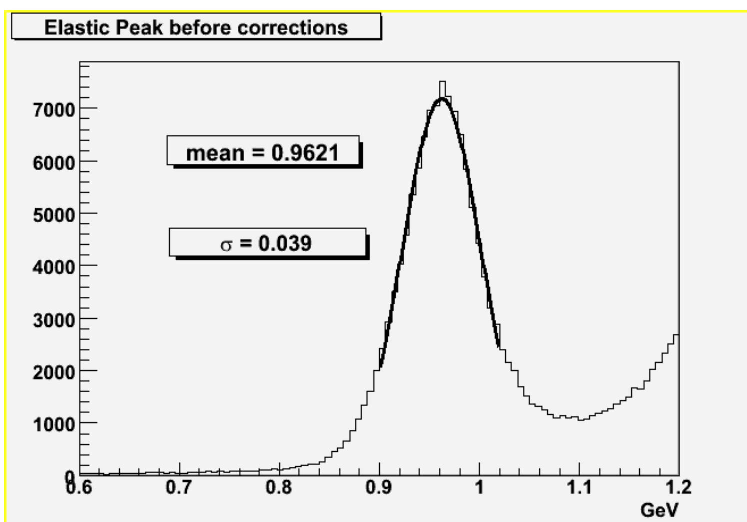

Figure 1.7: Elastic peak before corrections

1.2.2 Fiducial cuts for hadrons

We apply cuts on inefficient zones also for hadrons. The form and parameters were developed in [6]. The cut is

$$\varphi_{min}[S] \leq \varphi_S \leq \varphi_{max}[S] \tag{1.3}$$

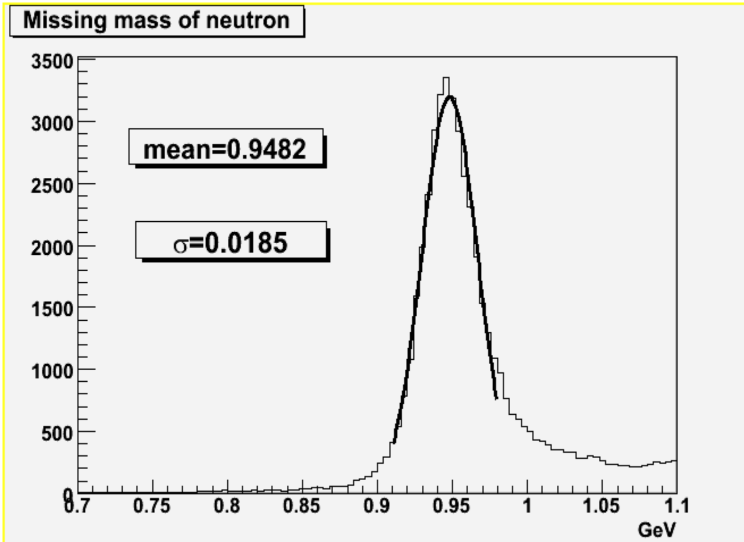

Figure 1.8: Neutron peak before corrections

where:

- S is the sector number
- $\varphi_{min}[S] = -a_{0m}[S] \times (1 - e^{-a_{1m}[S]\times(\theta - a_{2m}[s])}) + a_{3m}[s]$
- $\varphi_{max}[S] = -a_{0p}[S] \times (1 - e^{-a_{1p}[S]\times(\theta - a_{2p}[s])}) + a_{3p}[s]$

The parameters obtained for the e1-6 data set are listed in the table.

Table 1.1: The parameters for the hadron fiducial cuts

S	$a_{0p}[S]$	$a_{1p}[S]$	$a_{2p}[s]$	$a_{3p}[s]$	$a_{0m}[S]$	$a_{1m}[S]$	$a_{2m}[S]$	$a_{3m}[S]$
1	24.	0.22	8.	1.	25.	0.22	8.	1.
2	24.	0.23	8.	1.	26.	0.22	8.	1.
3	23.	0.20	8.	1.	26.	0.22	8.	1.
4	23.5	0.20	8.	1.	25.5	0.22	8.	1.
5	24.5	0.22	8.	1.	27.	0.16	8.	1.
6	24.5	0.22	8.	1.	26.	0.16	8.	1.

As in the case with electrons we need to impose additional fiducial cuts due to ineffective DC regions. On the Figures 1.15 and 1.16 there are examples of these cuts.

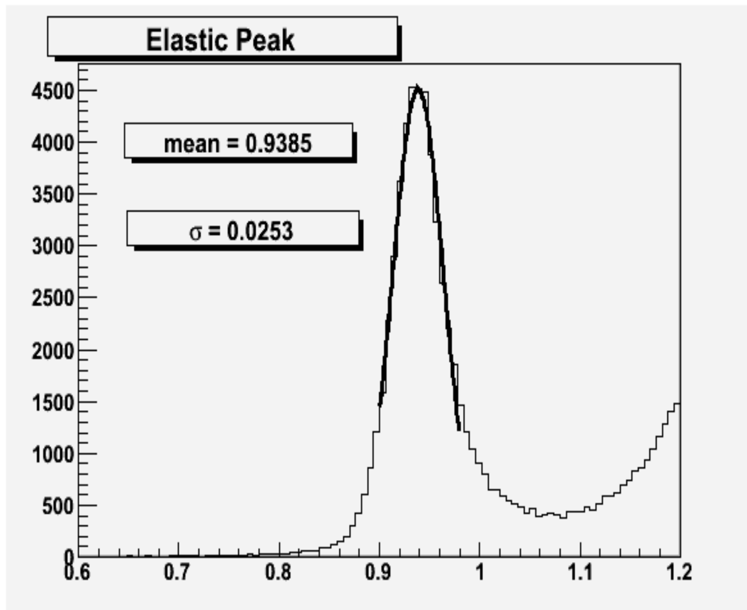

Figure 1.9: Elastic peak after corrections

1.2.3 Energy loss for protons

Detected recoil protons can lose a non negligible fraction of their energy, mostly in the target, in the air and in the DC. The measured momentum is then smaller than the momentum at the reaction point or vertex. The pions are mostly minimum ionizing, and their energy loss is neglected. For protons we used the correction procedure from [7], where the correction factors were derived using GSIM.

1.3 Exclusivity cut

After electron and hadron identification we ask for events with electron, proton and π^+. For these events we calculated $\pi^- X$ missing mass squared $M^2_{\pi^- X}$, which was determined as:

$$M^2_{\pi^- X} = (P_e + P_p - P_{e'} - P_{\pi^+} - P_{p'})^2 \tag{1.4}$$

To select the exclusive process ($ep \rightarrow e'p'\pi^+\pi^-$) we applied a cut over $M^2_{\pi^- X}$ (1.5), isolating the π^- peak. The distribution is shown on Fig. 1.17.

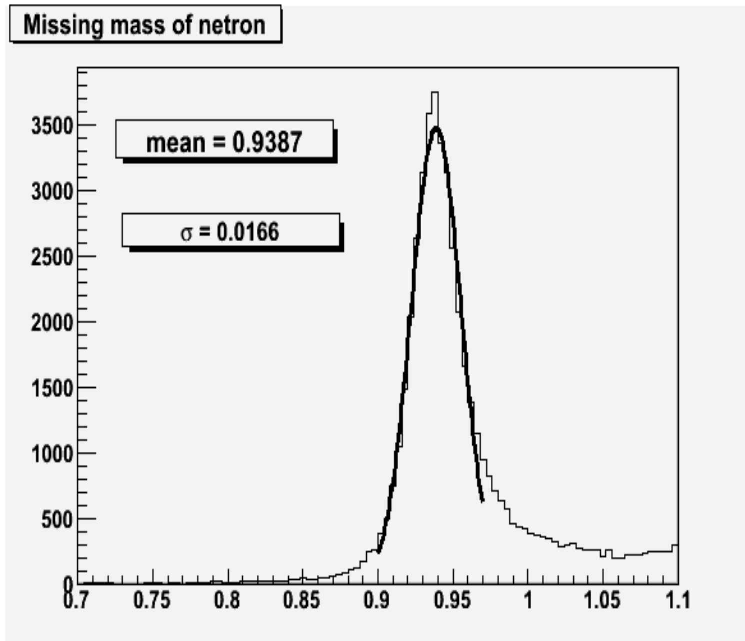

Figure 1.10: Neutron peak after corrections

The comparison of missing mass distribution between data events and Monte-Carlo events along with the cut lines

$$-0.04 < M^2_{\pi^- X} < 0.06 \text{ GeV}^2 \tag{1.5}$$

are shown on Fig. 1.18

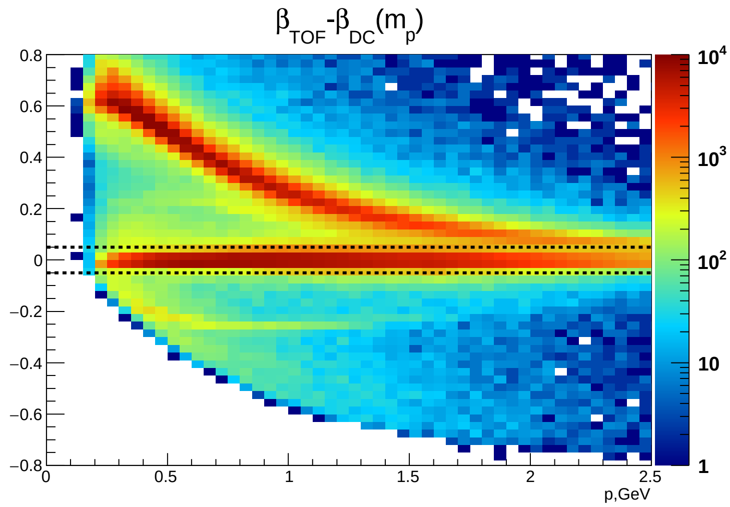

Figure 1.11: The $\Delta\beta(m)$ distribution assuming m is the proton mass.

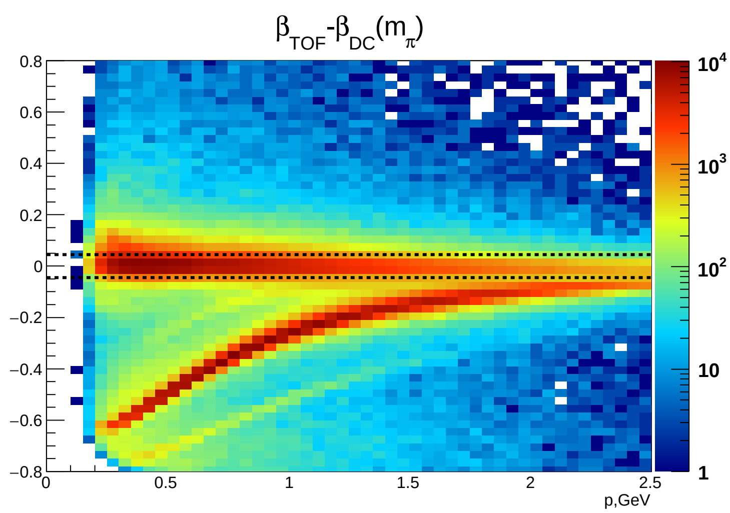

Figure 1.12: The $\Delta\beta(m)$ distribution assuming m is π^+ mass.

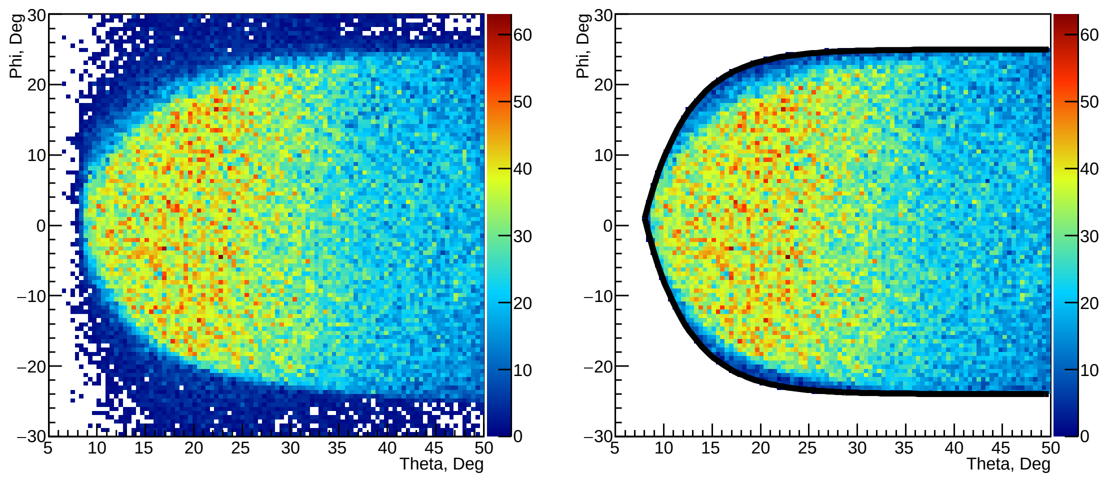

Figure 1.13: The protons ϕ versus θ distribution for sector 1.

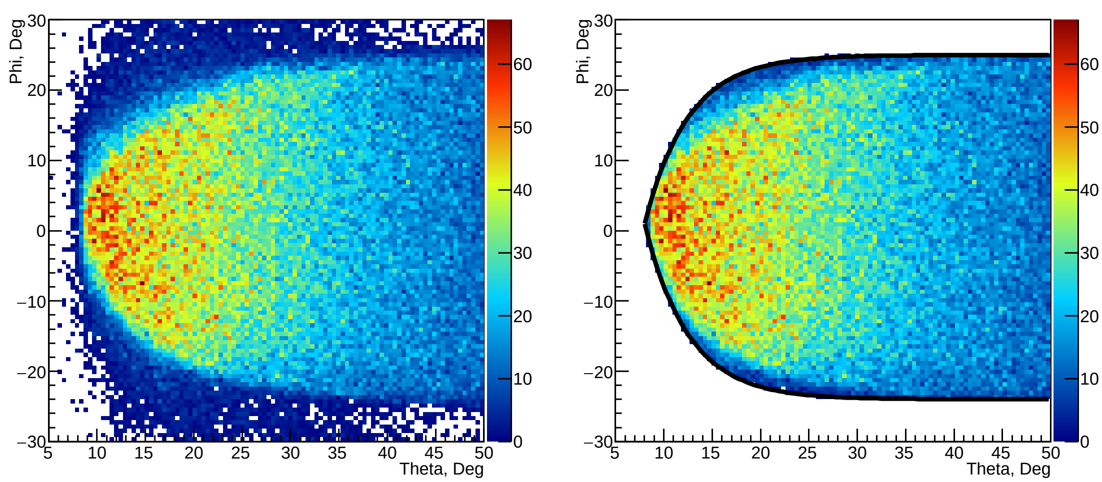

Figure 1.14: The positive pions ϕ versus θ distribution for sector 1.

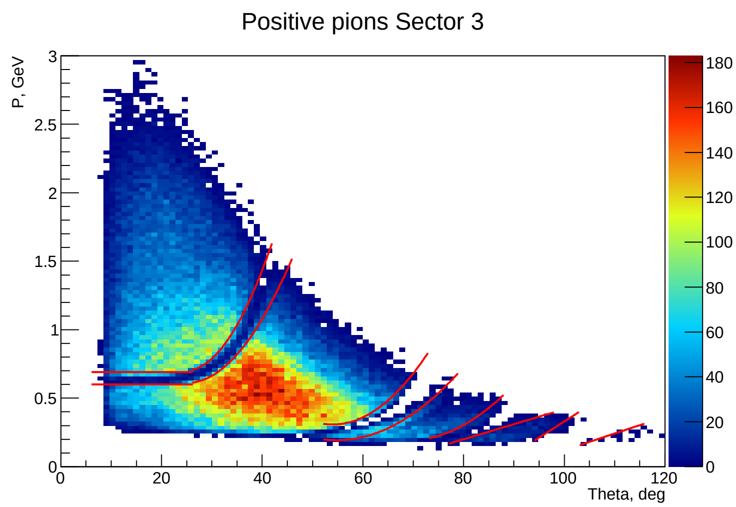

Figure 1.15: Positive pions: p vs θ distribution for sector 3 with additional fiducial cuts.

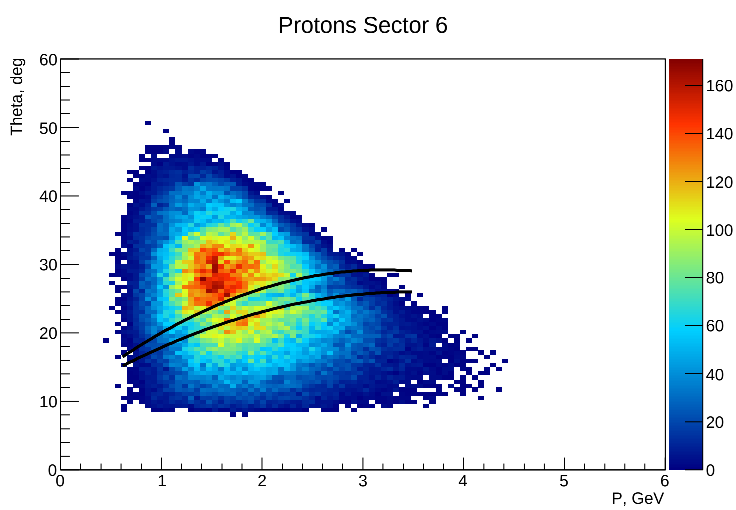

Figure 1.16: Protons: θ vs p distribution for sector 6 with additional fiducial cuts.

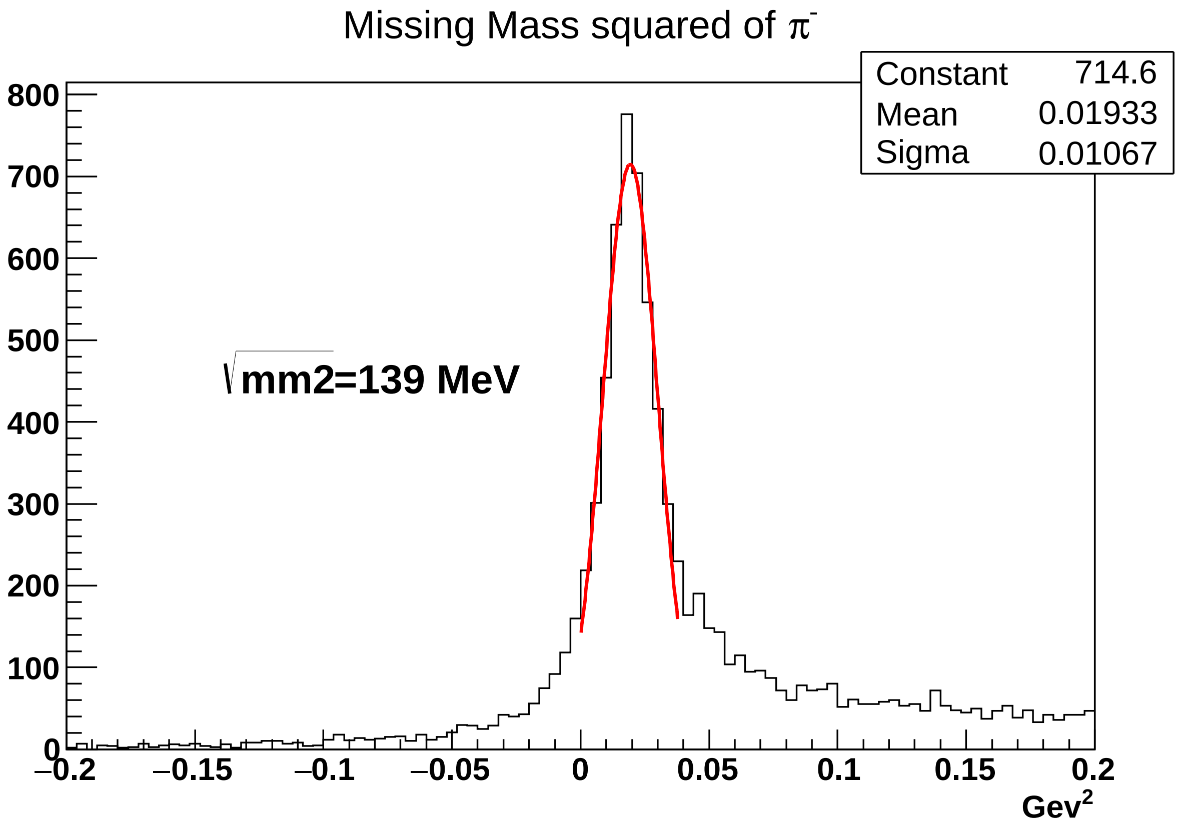

Figure 1.17: Missing mass squared of π^-.

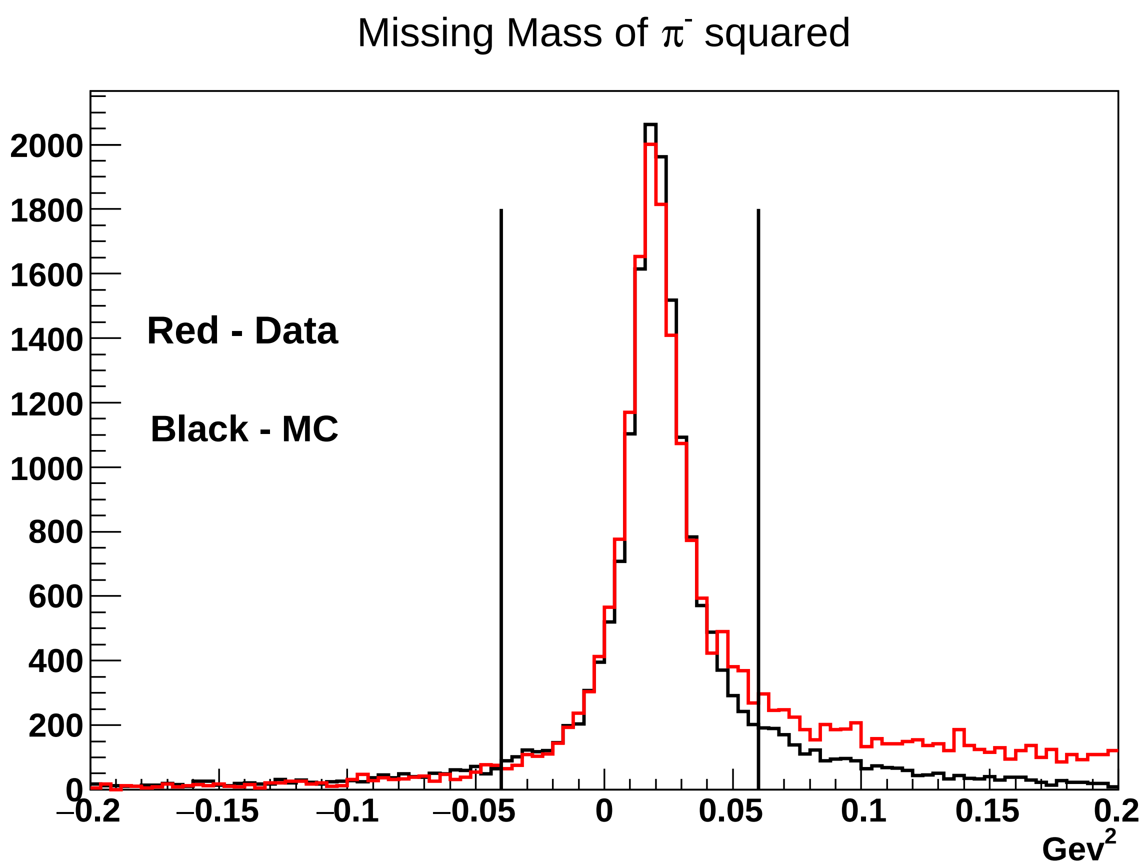

Figure 1.18: Missing mass squared of π^- with the cut lines. Red corresponds to data events. Black corresponds to Monte-Carlo.

Chapter 2

Cross-sections calculation

2.1 2π cross-section

The 3-body final state is unambiguously determined by 5 kinematics variables. Indeed, 3 final particles could be described by $4 \times 3 = 12$ components of theirs 4-momenta. All these particles are on-shell. So, it gives us 3 restrictions $E_i^2 - P_i^2 = m_i^2$ $(i = 1, 2, 3)$. Energy-momentum conservation imposes 4 additional constraints for the final particle four momentum components. So, eventually we remain with 5 kinematics variables, which determine unambiguously the 3-body final state kinematics. In the electron scattering process $ep \to ep'\pi^+\pi^-$ we also have variables W, Q^2 beyond the hadronic final state kinematics variables. So electron scattering cross sections for double charged pion production should be 7-differential: 5 variables for the final hadrons plus W and Q^2 determined by electron scattering kinematics. Such 7-differential cross sections may be written as $\frac{d^7\sigma}{dW dQ^2 d^5\tau}$, where $d^5\tau$ is 5-differential phase space, describing the final hadron kinematics.

Several sets of 5 variables for description of the final hadron kinematics may be used. We adopted the following set of variables:

- invariant mass of the first pair of particles M_{12};
- invariant mass of the second pair of particles M_{23};
- first particle solid angle Ω(in case of π^- see Fig. 2.1);
- the angle between two planes: one of them (plane A) is composed by 3-momenta of the virtual photon and first hadron; second plane (plane B) is composed by 3-momenta of two other hadrons (see Fig. 2.2).

Selected events were collected in 7-dimensional cells, corresponding to the variables: W, Q^2, invariant mass of first pairs of particles M_{12} and second pair of particles M_{23}, solid angle for the first final particle, the angle α between two planes. The cross sections were estimated in the CM frame. So, the four-momenta of the final particles described above, initially measured in lab frame, were boosted to the CM frame. We calculated cross section for various assignment for the first, second and third final hadrons:

- invariant mass of the $p\pi^+$ pair, invariant mass of the $\pi^+\pi^-$ pair, proton spherical angles θ_p and φ_p and angle $\alpha_{\pi^+\pi^-}$ between planes B (composed by momenta of $\pi^+\pi^-$ pair) and A (composed by initial and final protons);

- invariant mass of the $\pi^-\pi^+$ pair, invariant mass of the π^+p pair, π^- spherical angles θ_{π^-} and φ_{π^-} and angle $\alpha_{p\pi^+}$ between planes B (composed by momenta of $p\pi^+$ pair) and A (composed by initial proton and π^-);

- invariant mass of the $\pi^+\pi^-$ pair, invariant mass of the π^-p pair, π^+ spherical angles θ_{π^+} and φ_{π^+} and angle $\alpha_{p\pi^-}$ between planes B (composed by momenta of $p\pi^-$ pair) and A (composed by initial proton and π^+).

The final particle emission angles for the second set of variables is shown on Fig. 2.1.

Cross sections calculated in these variables were used in physics analysis. The variables $(M_{\pi^+\pi^-}, M_{\pi^+p}, \theta_{\pi^-}, \varphi_{\pi^-}, \alpha_{\pi^+p})$ were calculated from 3-momenta of the final particles $\vec{P}_{\pi^-}$, $\vec{P}_{\pi^+}$, $\vec{P}_{p'}$ in the following way. Since all observables are measured in the lab frame, first we transfer 3-momenta of the final particles in the CM frame. All 3-momenta used below, if not specified otherwise, are defined in c.m. frame. The $M_{\pi^+\pi^-}$, M_{π^+p} and M_{π^-p} invariant masses are related to four momenta of the final particles as:

$$\begin{aligned} M_{\pi^+\pi^-} &= \sqrt{(P_{\pi^+} + P_{\pi^-})^2} \\ M_{\pi^+p'} &= \sqrt{(P_{\pi^+} + P_{p'})^2} \\ M_{\pi^-p'} &= \sqrt{(P_{\pi^-} + P_{p'})^2}\ , \end{aligned} \tag{2.1}$$

where P_i stand for the final particle four-momentum.

The angle θ_{π^-} between 3-momentum of the initial photon and final π^- in the CM frame is calculated as:

$$\theta_{\pi^-} = acos\left(\frac{(\vec{P}_{\pi^-}\vec{P}_{\gamma})}{|\vec{P}_{\pi^-}||\vec{P}_{\gamma}|}\right) \tag{2.2}$$

The φ_{π^-} angle is determined as:

$$\varphi_{\pi^-} = arctg\left(\frac{P_{y\pi^-}}{P_{x\pi^-}}\right); \quad P_{x\pi^-} > 0; P_{y\pi^-} > 0 \tag{2.3}$$

$$\varphi_{\pi^-} = arctg\left(\frac{P_{y\pi^-}}{P_{x\pi^-}}\right) + 2\pi; \quad P_{x\pi^-} > 0; P_{y\pi^-} < 0 \tag{2.4}$$

$$\varphi_{\pi^-} = arctg\left(\frac{P_{y\pi^-}}{P_{x\pi^-}}\right) + \pi; \quad P_{x\pi^-} < 0; P_{y\pi^-} < 0 \tag{2.5}$$

$$\varphi_{\pi^-} = arctg\left(\frac{P_{y\pi^-}}{P_{x\pi^-}}\right) + \pi; \quad P_{x\pi^-} < 0; P_{y\pi^-} > 0 \tag{2.6}$$

$$\varphi_{\pi^-} = \pi/2; \quad P_{x\pi^-} = 0; P_{y\pi^-} > 0 \tag{2.7}$$

$$\varphi_{\pi^-} = 3\pi/2; \quad P_{x\pi^-} = 0; P_{y\pi^-} < 0 \tag{2.8}$$

The calculation of angle α_{π^+p}, between two planes A and B (see Fig. 2.2), is more complicated. First we determine two auxiliary vectors $\vec{\gamma}$ and $\vec{\beta}$. The vector $\vec{\gamma}$ is a unit vector perpendicular to the 3-momentum $\vec{P}_{\pi^-}$, directed toward the vector $-\vec{n}_z$ and situated in the plane composed by the virtual photon 3-momentum and 3-momentum $\vec{P}_{\pi^-}$ (see Fig. 2.2). $\vec{n}_z$ is the unit vector directed along z-axis (see Fig. 2.2). The vector $\vec{\beta}$ is the unit vector perpendicular to the 3-momentum of π^-, directed toward the 3-momentum $\vec{P}_{\pi^+}$ and situated in the plane composed by the π^+ and p' 3-momenta. Note that the 3-momenta of π^+, π^- and p' are in the same plane, since in the CM their total 3-momentum should be equal to zero. Then the angle between two planes α_{π^+p} is:

$$\alpha_{\pi^+p} = acos(\vec{\gamma}\vec{\beta}) \tag{2.9}$$

where the *acos* function is running between zero and π. From the other hand, the angle between the planes A and B may vary between zero and 2π. To determine the α angle in a range between π and 2π we look at the relative direction of the vector $\vec{P}_{\pi^-}$ and vector product $\vec{\delta}$ for mentioned above auxiliary vectors $\vec{\gamma}$ and $\vec{\beta}$:

$$\vec{\delta} = \vec{\gamma} \times \vec{\beta} \tag{2.10}$$

If the vector $\vec{\delta}$ was collinear to $\vec{P}_{\pi^-}$, the α_{π^+p} angle is determined from (2.9). In the case of anti collinear vectors $\vec{\delta}$ and $\vec{P}_{\pi^-}$:

$$\alpha_{\pi^+p} = 2\pi - acos(\vec{\gamma}\vec{\beta}) \tag{2.11}$$

Defined above, the vector $\vec{\gamma}$ may be expressed through the particle 3-momenta as:

$$\begin{aligned} \vec{\gamma} &= a_\alpha(-\vec{n}_z) + b_\alpha \vec{n}_{P_{\pi^-}} \\ a_\alpha &= \sqrt{\frac{1}{1-(\vec{n}_{P_{\pi^-}}(-\vec{n}_z))^2}} \\ b_\alpha &= -(\vec{n}_{P_{\pi^-}}(-\vec{n}_z))a_\alpha \ , \end{aligned} \tag{2.12}$$

where $\vec{n}_{P_{\pi^-}}$ is the unit vector directed along the $\vec{P}_{\pi^-}$ 3-momentum (see Fig. 2.2). Taking scalar products $(\vec{\gamma}\vec{n}_{P_{\pi^-}})$ and $(\vec{\gamma}\vec{\gamma})$, it is straightforward to verify, that the $\vec{\gamma}$ is the unit vector perpendicular to $\vec{P}_{\pi^-}$. Vector $\vec{\beta}$ may be obtained as:

$$\begin{aligned} \vec{\beta} &= a_\beta \vec{n}_{P_{\pi^+}} + b_\beta \vec{n}_{P_{\pi^-}} \\ a_\beta &= \sqrt{\frac{1}{1-(\vec{n}_{P_{\pi^+}}\vec{n}_{P_{\pi^-}})^2}} \\ b_\beta &= -(\vec{n}_{P_{\pi^+}}\vec{n}_{P_{\pi^-}})a_\beta \ , \end{aligned} \tag{2.13}$$

where $\vec{n}_{P_{\pi^+}}$ is the unit vector directed along the $\vec{P}_{\pi^+}$ 3-momentum. Again taking scalar products $(\vec{\beta}\vec{n}_{P_{\pi^-}})$ and $(\vec{\beta}\vec{\beta})$, it is straightforward to see that $\vec{\beta}$ is the unit vector perpendicular to the π^- 3-momentum. The Angle α_{π^+p} coincides with angles between vectors $\vec{\gamma}$ and $\vec{\beta}$. So, the scalar product $(\vec{\gamma}\vec{\beta})$ allows us to determine the angle α_{π^+p} (2.9). The kinematics variables for the other hadron assignment for the first, second and third final particles described above were evaluated in a similar way.

For the second set of kinematics variables, 7-differential cross section may be written as: $\frac{d\sigma}{dWdQ^2dM_{p\pi^+}dM_{\pi^+\pi^-}d\Omega_{\pi^-}d\alpha_{p\pi^+}}$. These cross sections were calculated from the quantity of selected events collected in the respective 7-differential cell and using estimated values of full efficiency F as:

$$\frac{d\sigma}{dWdQ^2dM_{p\pi^+}dM_{\pi^+\pi^-}d\Omega d\alpha_{p\pi^+}} = \frac{1}{F\cdot R}\frac{\left(\frac{\Delta N}{Q_{tot}}\right)}{\Delta W\Delta Q^2\Delta\tau\left(\frac{l_t D_t N_A}{q_e M_H}\right)} \ , \tag{2.14}$$

where ΔN are the numbers of events inside the 7-dimensional bin, and F is the full efficiency coming from the Monte Carlo simulations. $F = Acc \times Eff$, where Acc is the fraction of events which passed fiducial cuts for the electron. For efficiency we used events which satisfy slightly wider fiducial cuts and then passed them to GSIM. This is done for saving computer time, because the simulation in GSIM is the most time consuming operation. R is the radiative correction factor; for details see Chapter 3, Q_{tot} is the integrated Faraday Cup charge for run with hydrogen and, q_e is the elementary charge ($q_e = 1.610^{-19}$C), D_t is the density of hydrogen ($D_t = 0.073$ gr/cm^3), l_t is the length of the target ($l_t = 5$ cm), M_H is the molar density of hydrogen ($M_H = 1$ gr/mol), N_A is Avogadro's number ($N_A = 6.0210^{23}$ mol^{-1}), ΔW and ΔQ^2 are determined by electron scattering kinematics, were bins and $\Delta\tau$ is element of the hadronic 7-dimensional phase space:

$$\Delta\tau = \Delta M_{p\pi^+} \Delta M_{\pi^+\pi^-} \Delta cos(\theta_{\pi^-}) \Delta\varphi_{\pi^-} \Delta\alpha_{p\pi^+} \tag{2.15}$$

In the single photon exchange approximation, the electron scattering cross section is related to the hadronic cross section $\frac{d\sigma}{dM_{p\pi^+} dM_{\pi^+\pi^-} d\Omega_{\pi^-} d\alpha_{p\pi^+}}$ as:

$$\frac{d\sigma}{dM_{p\pi^+} dM_{\pi^+\pi^-} d\Omega_{\pi^-} d\alpha_{p\pi^+}} = \frac{1}{\Gamma_v} \frac{d\sigma}{dW dQ^2 dM_{p\pi^+} dM_{\pi^+\pi^-} d\Omega_{\pi^-} d\alpha_{p\pi^+}} \ , \tag{2.16}$$

where Γ_v is the virtual photon flux, given by

$$\Gamma_v = \frac{\alpha}{4\pi} \frac{1}{E_{beam}^2 M_p^2} \frac{W(W^2 - M_p^2)}{(1-\varepsilon)Q^2} \ , \tag{2.17}$$

where α is the fine structure constant, M_p is the proton mass and ε is the virtual photon transverse polarization, given by

$$\varepsilon = \left(1 + 2\left(1 + \frac{\omega^2}{Q^2}\right) tan^2\left(\frac{\theta_e}{2}\right)\right)^{-1} \ , \tag{2.18}$$

were $\omega = E_{beam} - E_{scattered\ electron}$, and θ_e is the electron scattering angle in the lab frame. W, Q^2 and θ_e were taken in the center of the bin.

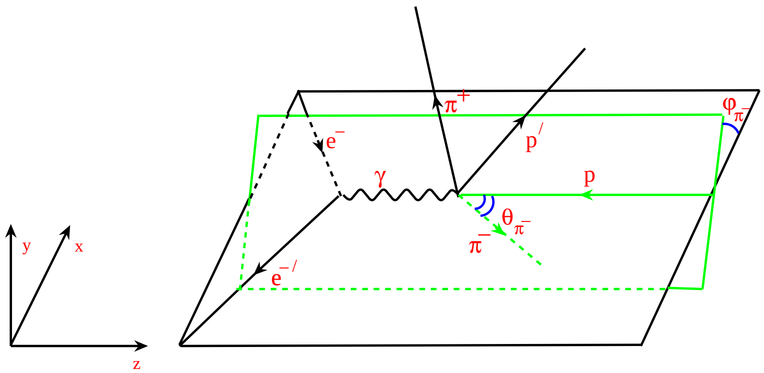

Figure 2.1: Kinematics of $\pi^+\pi^-$ electroproduction

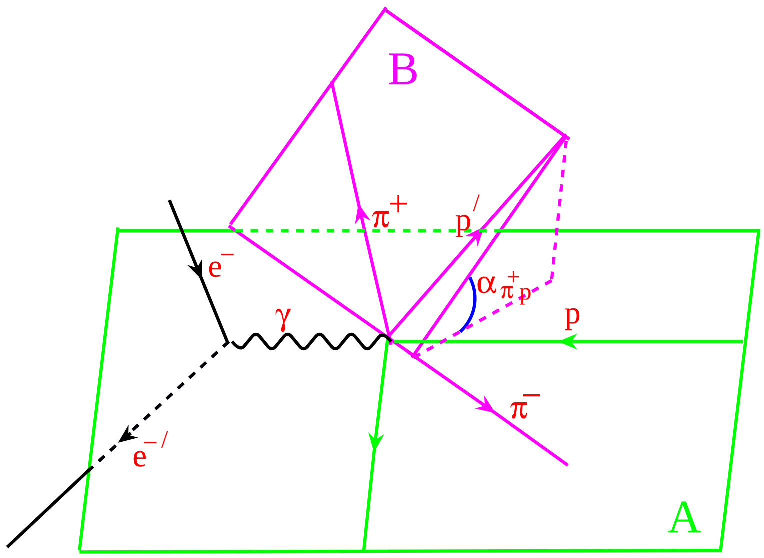

Figure 2.2: Tha α angle between two planes

Limited statistics does not allow us to estimate the 5-differential cross section with reasonable accuracy. Moreover at the first step of physics analysis, aimed to determine the contributing mechanisms, it is even beneficial to use the single differential cross-sections, since the structures and steep evolution of these cross-sections may be directly related to a particular meson-baryon mechanism. So, we analyzed sets of single differential cross sections, obtained after integration of the 5-differential cross sections over 4 variables. We obtained the following set of 1-differential 2π cross sections:

$$
\begin{aligned}
\frac{d\sigma}{dM_{\pi^+\pi^-}} &= \int \frac{d^5\sigma}{d^5\tau} d\tau_{\pi^+\pi^-}; \qquad d\tau_{\pi^+\pi^-} = dM_{\pi^-p} d\Omega_{\pi^-} d\alpha_{p\pi^+} \\
\frac{d\sigma}{dM_{\pi^+p}} &= \int \frac{d^5\sigma}{d^5\tau} d\tau_{\pi^+p}; \qquad d\tau_{\pi^+p} = dM_{\pi^+\pi^-} d\Omega_{\pi^-} d\alpha_{p\pi^+} \\
\frac{d\sigma}{d(-cos\theta_{\pi^-})} &= \int \frac{d^5\sigma}{d^5\tau} d\tau_{\pi^-}; \quad d\tau_{\pi^-} = dM_{\pi^+\pi^-} dM_{\pi^+p} d\varphi_{\pi^-} d\alpha_{p\pi^+} \\
\frac{d\sigma}{dM_{\pi^-p}} &= \int \frac{d^5\sigma}{d^5\tau'} d\tau_{\pi^-p}; \qquad d\tau_{\pi^-p} = dM_{\pi^+\pi^-} d\Omega_{\pi^+} d\alpha_{p\pi^-} \\
d^5\tau' &= dM_{\pi^-p} dM_{\pi^+\pi^-} d\Omega_{\pi^+} d\alpha_{p\pi^-}
\end{aligned}
\tag{2.19}
$$

In the actual cross section calculations the integrals in (2.19) are substituted by the respective sums over the 5-dimensional kinematics grid for hadronic cross sections. To evaluate absolute statistical error of 5-differential hadronic cross sections we used an error propagation approach:

$$
\delta_{stat}(M_{p\pi^+}, M_{\pi^+\pi^-}, \theta_{\pi^-}, \varphi_{\pi^-}, \alpha_{p\pi^+}) = \frac{1}{F \cdot R} \frac{1}{\Gamma_v} \frac{\sqrt{\left(\frac{\Delta N}{Q^2_{tot}}\right)}}{\Delta W \Delta Q^2 \Delta\tau \left(\frac{l_t D_t N_A}{q_e M_H}\right)}
\tag{2.20}
$$

Another source of statistical fluctuations is connected to the statistics in the Monte Carlo: from formula (2.14), it is clear that the error in the knowledge of the efficiency is affecting the cross section value. Here we have to spend a few words about the statistical error in the simulation; the definition of the efficiency factor is

$$
Eff = \frac{N_{rec}}{N_{gen}}. \tag{2.21}
$$

The absolute statistical error on Eff is given by

$$
\delta(Eff) = \sqrt{\frac{N_{rec}(N_{gen} - N_{rec})}{N^3_{gen}}}. \tag{2.22}
$$

The error on the cross section due to the limited Monte Carlo statistic is given by

$$\delta_{stat,Eff} = \frac{d\sigma}{dM_{p\pi^+}dM_{\pi^+\pi^-}d\Omega d\alpha_{p\pi^+}}\left(\frac{\delta(Eff)}{Eff}\right) \tag{2.23}$$

Also we have the acceptance which gives us the portion of events that passed the fiducial cuts for the electron. We estimate the statistical error the same way as the error on the efficiency. Finally we combined quadratically the statistical errors coming from the fluctuations in the data and from the Monte Carlo, so the total absolute statistical error is given by

$$\delta_{stat,tot} = \sqrt{\delta^2_{stat} + \delta^2_{stat,Eff} + \delta^2_{stat,Acc}}. \tag{2.24}$$

2.2 Acceptance and efficiency evaluation

We use the *genev* Monte Carlo event generator(EG) of the Genova group (M. Ripani, E. Golovach et al.). This event generator is capable to simulate the event distribution for major meson photo and electroproduction channels in the N* excitation region. The parameter list for the EG includes various kinematical parameters(W, Q^2, electron angles and so on), target parameters(length, offset). This EG can also generate radiative effects, calculated according to [8]. The event generator is based on the JM06 [9] model. In order to save time we decided to calculate the detector response in two steps. First we generate events in the entire phase space of the reaction and then apply the electron fiducial cuts. This gives us the acceptance tables. Second we generate events inside the electron fiducial cuts(in fact they satisfy a little wider cuts) and then pass them to GSIM. GSIM (Geant Simulation) is the program which uses Geant3 libraries and fully simulates the subsystems of the CLAS detector. A configuration file specifying the information about parts of the detector, target and magnetic field is needed to run GSIM. This file, called $ffreadcard$ is given below.

```

CUTS   5.e-3 5.e-3 5.e-3 5.e-3 5.e-3
CCCUTS 1.e-3 1.e-3 1.e-3 1.e-3 1.e-3
DCCUTS 1.e-4 1.e-4 1.e-4 1.e-4 1.e-4
ECCUTS 1.e-4 1.e-4 1.e-4 1.e-4 1.e-4
SCCUTS 1.e-4 1.e-4 1.e-4 1.e-4 1.e-4

RUNG   1
```

```
GEOM   'ALL '
NOGEOM 'PTG' 'ST  '
UPSTPOS 0.0 0.0 0.0

MAGTYPE  3
MAGSCALE 0.874352 0.75
FIELD    2

CHAMBER 2
TARGET  'e1-6'
TGMATE  'HYDR'
TGPOS   0.0 0.0 -4.0

NOMCDATA 'ALL'

AUTO 1

STOP
```

To process generated events with GSIM takes most of the computer time, that is why we use this two-step procedure. After GSIM we run the GPP program which smears the response from the GSIM programmed detector. Several input parameters should be given to GPP which is a DC smearing factor(for 3 regions: a,b,c) and a TOF smearing factor(one constant f). We derived the DC smearing factors from the condition that the missing mass squared distribution of the π^- have the same width in simulation and in real data. We use the following values $a = b = c = 2.25$, $f = 1.3$. Then the output file is reconstructed with the RECSIS program using CALDB RunIndexe1_6. So looking at reconstructed events we can compare the behavior of the real data and MC data after the chain of programs. We would like to have similar shapes of the distributions in MC and in data. So we adjusted the event generator to the data introducing correction factors. The correction factors were the ratios of events from data and reconstructed events from MC. We derived these factors for each 4 dimensional bin in $Q^2, W, M_{\pi^+\pi^-}, M_{\pi^+p}$.

The quality of the adjustment can be seen on the following Figures (2.3, 2.4...). We have about 400 million events generated in the entire phase space for acceptance evaluation and about 100 million events generated in the fiducial cuts region for efficiency evaluation. We use the scheme where we have acceptance and efficiency with the full detector response function being the product of the acceptance and the efficiency. We don't use the usual CC photoelectrons cut, instead we apply CC matching cuts which proved to be working in data and in MC[15]. Since we don't see any unexpected structures/jumps in kinematics dependencies of one-fold differential cross sections, we decided that MC evaluation of efficiency is well suited for evaluation of 1-diff cross sections and do not implement any additional cuts on the 5d cells of small efficiencies.

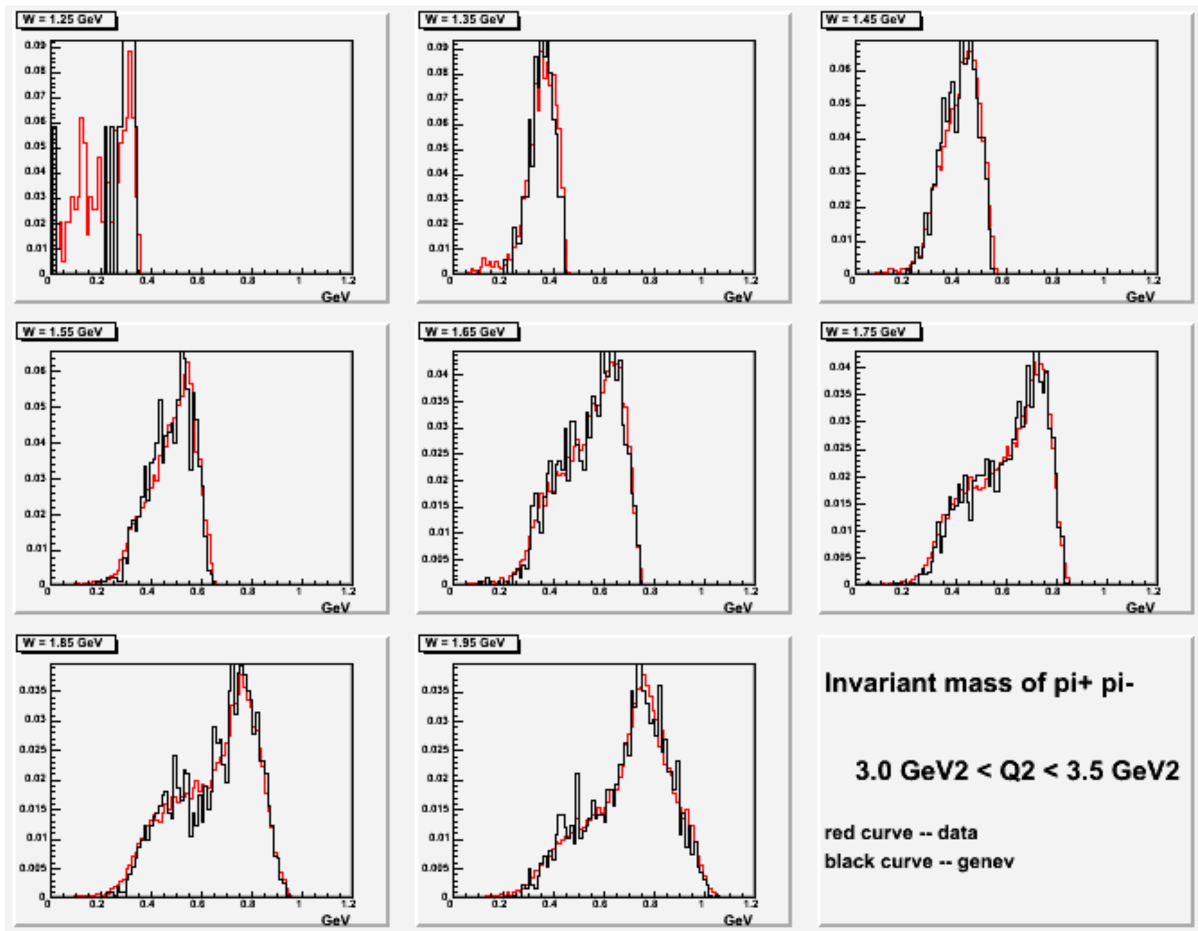

Figure 2.3: The $\pi^+\pi^-$ invariant mass distribution. Red - data events. Black - reconstructed from MC events. Our kinematics starts at $W = 1.40$ GeV, so the top left graph is of no concern.

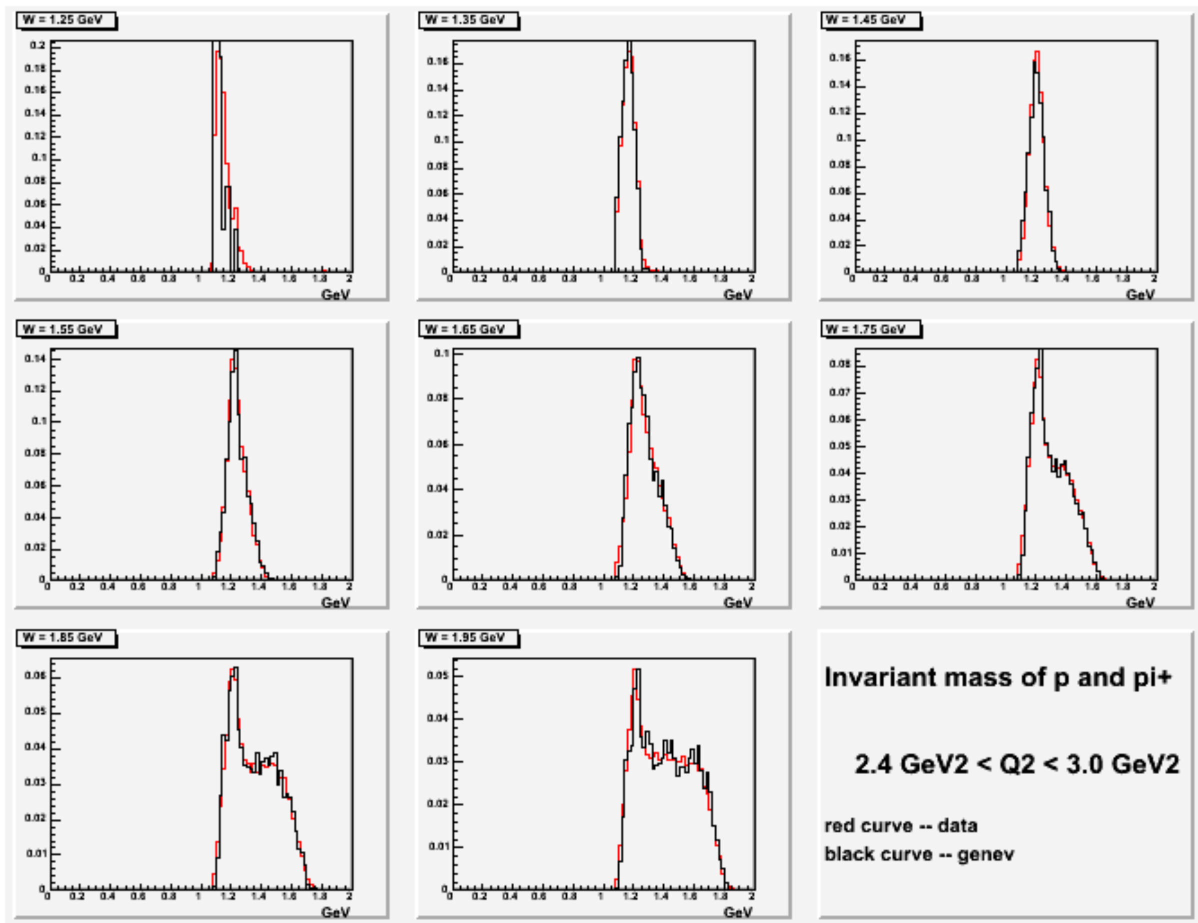

Figure 2.4: The invariant mass distribution of proton and π^+. Red - data events. Black - reconstructed from MC events

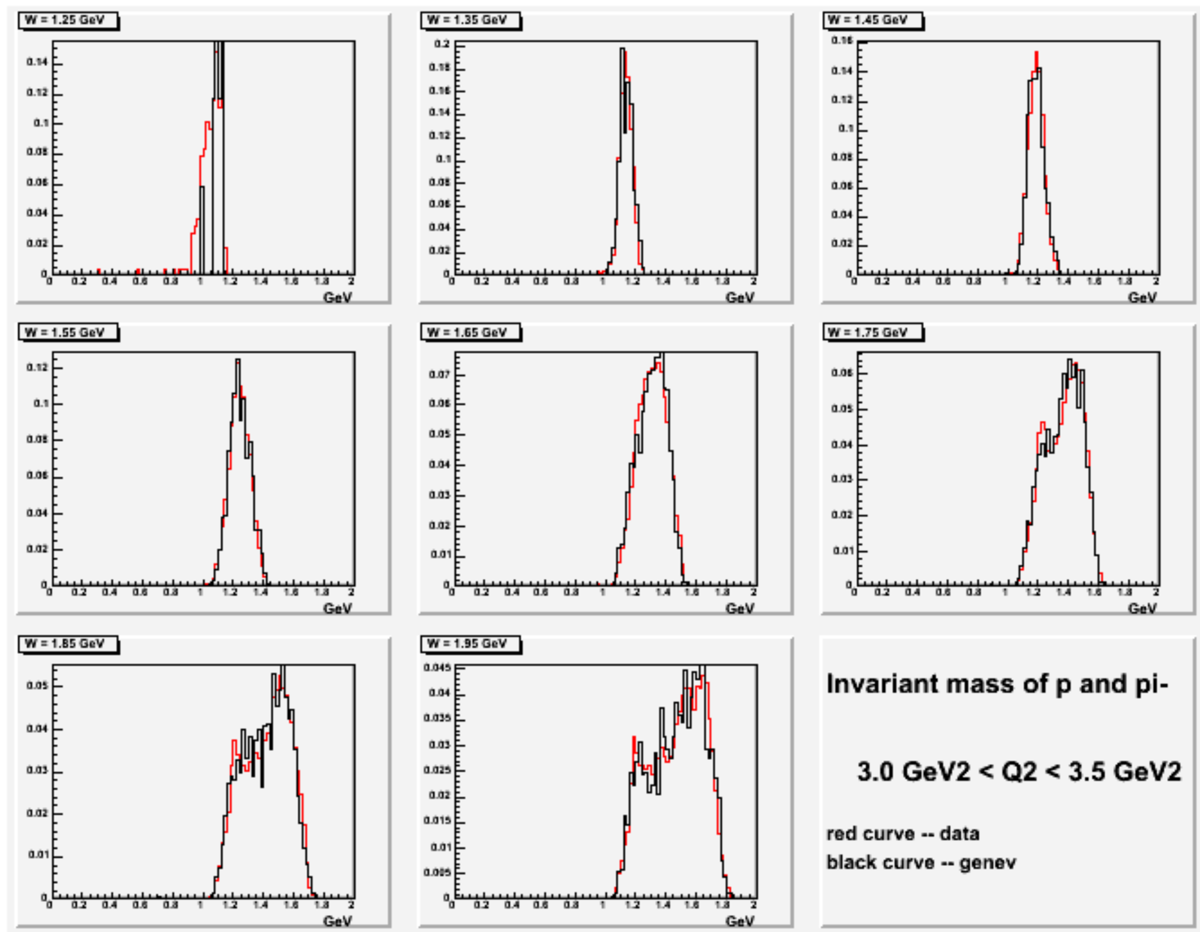

Figure 2.5: The invariant mass distribution of proton and π^-. Red - data events. Black - reconstructed from MC events

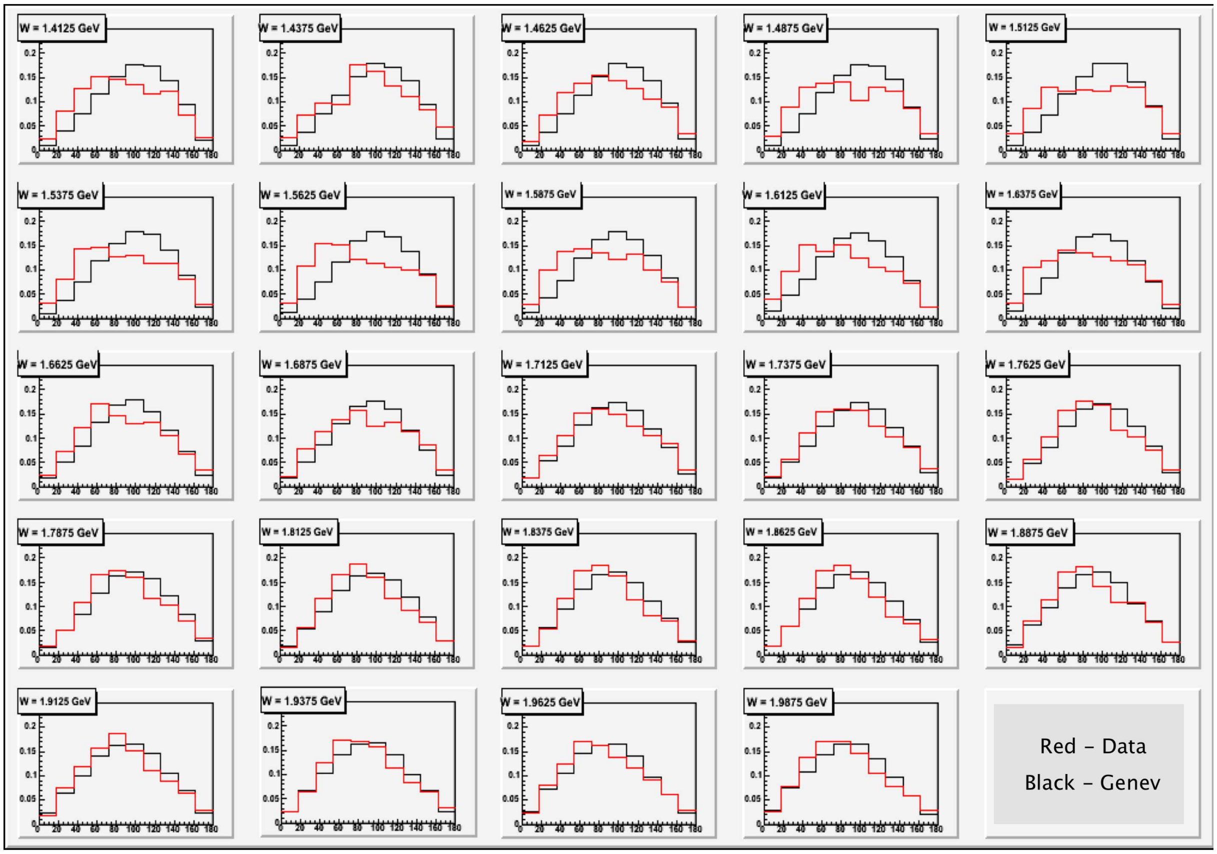

Figure 2.6: The polar angle of π^- in CM distribution. Red - data events. Black - reconstructed from MC events

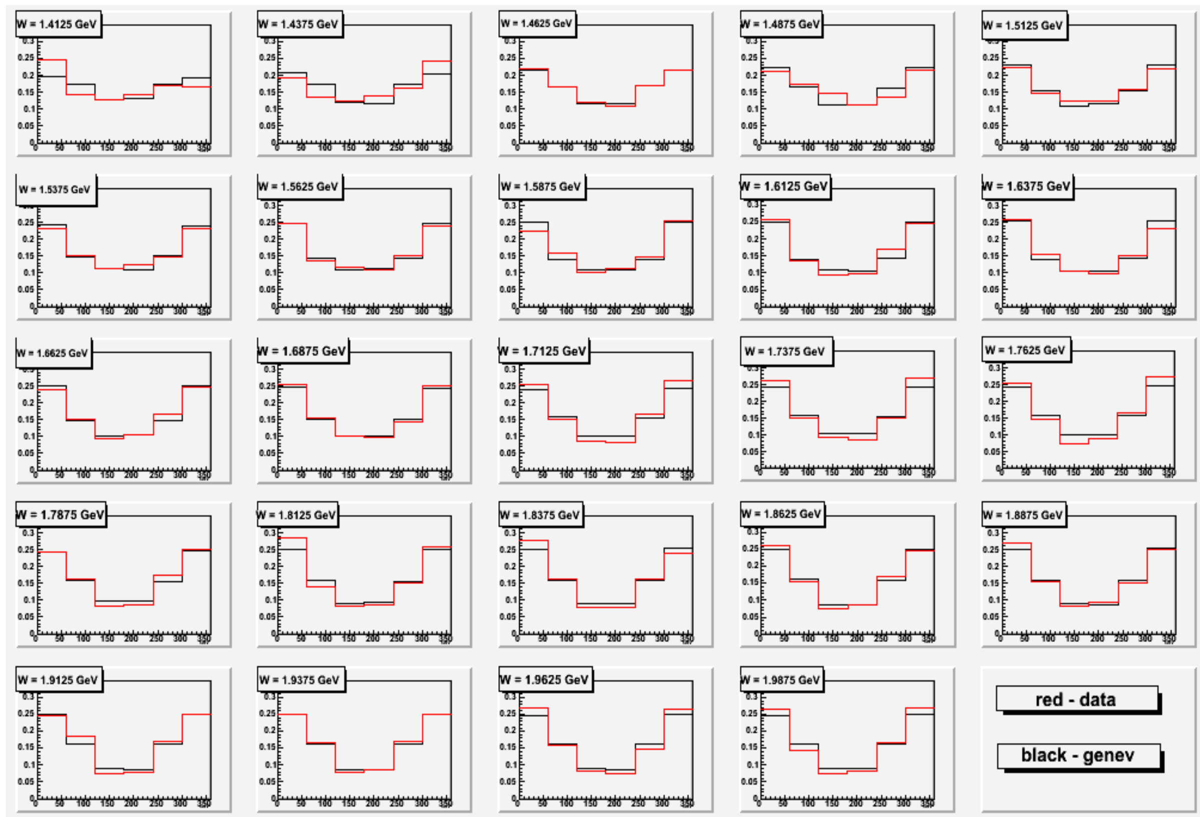

Figure 2.7: The azimuthal angle of π^- in CM distribution. Red - data events. Black - reconstructed from MC events

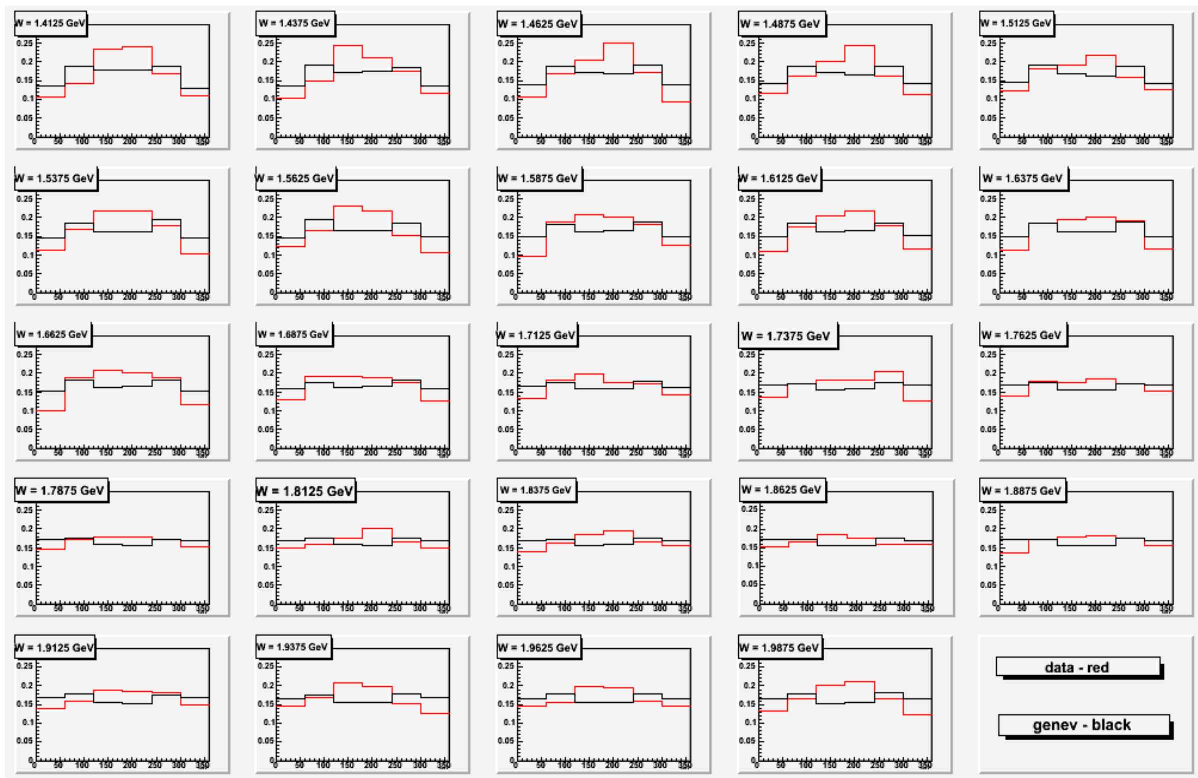

Figure 2.8: Angle between 2 planes($\gamma\pi^-$ and π^+p). Red - data events. Black - reconstructed from MC events

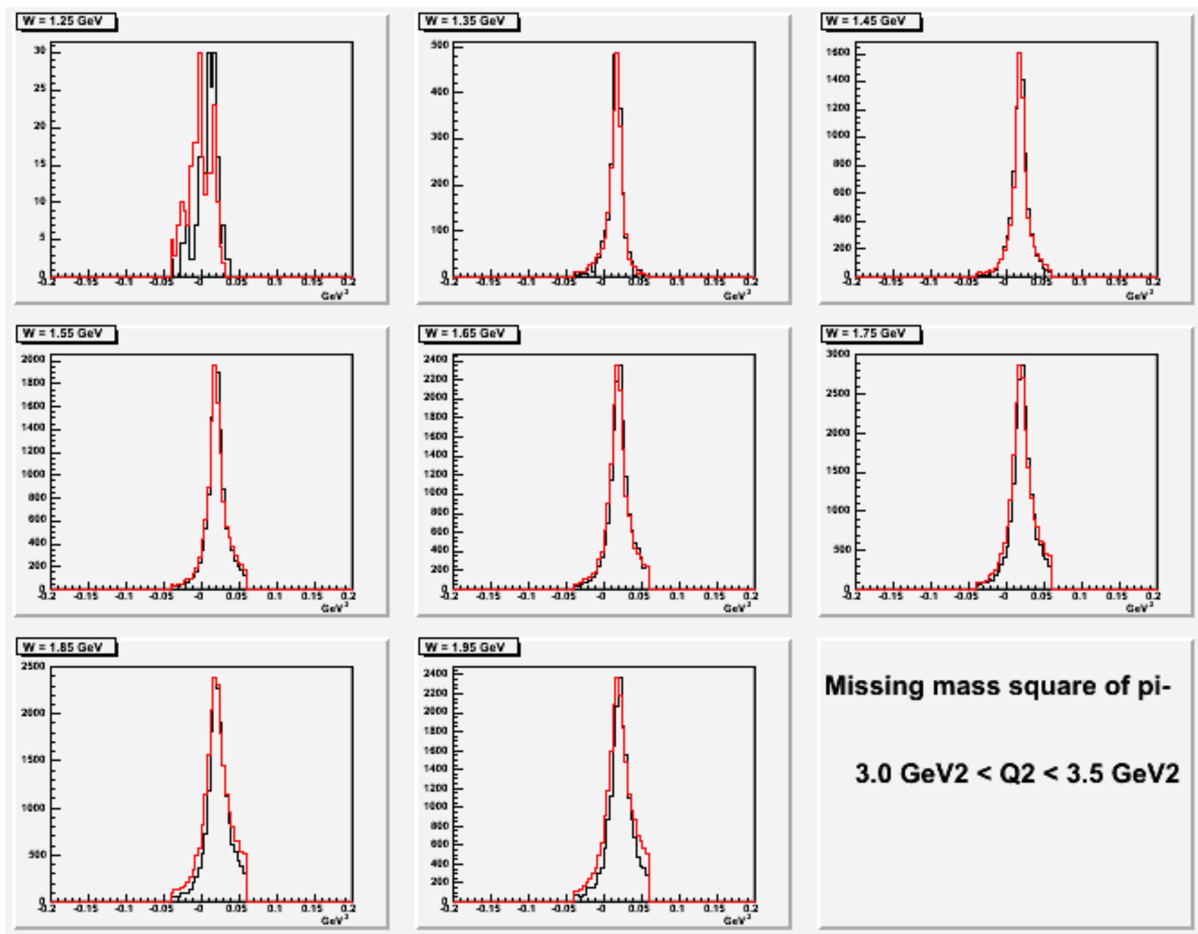

Figure 2.9: Missing mass squared of π^-. Red - data events. Black - reconstructed from MC events

2.3 Interpolation of cross sections into the kinematics areas corresponded to blind zones("holes" in the acceptance)

In the data analysis we found kinematics for which we have simulated events, while the quantity of accepted events was equal to zero. Such situation represent an indication of zero CLAS detector acceptance in these kinematics regions. We need to account for the contribution of such blinded area to the integrals (2.19) for the single differential cross sections.

To estimate the contributions to the cross sections from CLAS blinded areas we used information from the event generator. We evaluated such contributions based on the cross section description of the modified Genova event generator, as described in section 2.2. To obtain the 5-differential virtual photon cross sections in the blind areas $\frac{d\sigma}{dM_{p\pi^+}dM_{\pi^+\pi^-}d\Omega_{\pi^-}d\alpha_{p\pi^+}}$, we used as input: the number of measured events in current (W, Q^2) bin integrated over all hadronic variables for the $\pi^+\pi^-p$ final state $N_{data,int}$; the number of these events estimated from event generator $N_{generated,int}$; the number of generated events in 7-D cell $(W, Q^2, M_{p\pi^+}, \Omega_{\pi^-}, \alpha_{\pi^+,p})$ $N^{7D}_{generated}$. Using the event generator as a guide, we estimated the quantity of events in the blinded cell as $\frac{N_{data,int}}{N_{generated,int}}N^{7D}_{generated}$. So, the 5-differential cross sections in the blinded area were calculated as:

$$\frac{d\sigma}{dM_{p\pi^+}dM_{\pi^+\pi^-}d\Omega d\alpha_{p\pi^+}} = \frac{1}{R\Gamma_v}\frac{\left(\frac{1}{F_{int}}\frac{N_{data,int}}{N_{generated,int}}N^{7D}_{generated}\right)/Q_{tot}}{\Delta W\Delta Q^2\Delta\tau\left(\frac{l_tD_tN_A}{q_eM_H}\right)}\ , \tag{2.25}$$

where F_{int} is integral efficiency inside 5-D bin, Q_{tot} is the integrated Faraday Cup charge.

An example of when cross-sections were calculated with the blind zones filled and without filling is given in Fig. 2.10. Of course such corrections depends on the event generator and are therefore model dependent. We take that into account by assigning systematic uncertainty(see 4.5).

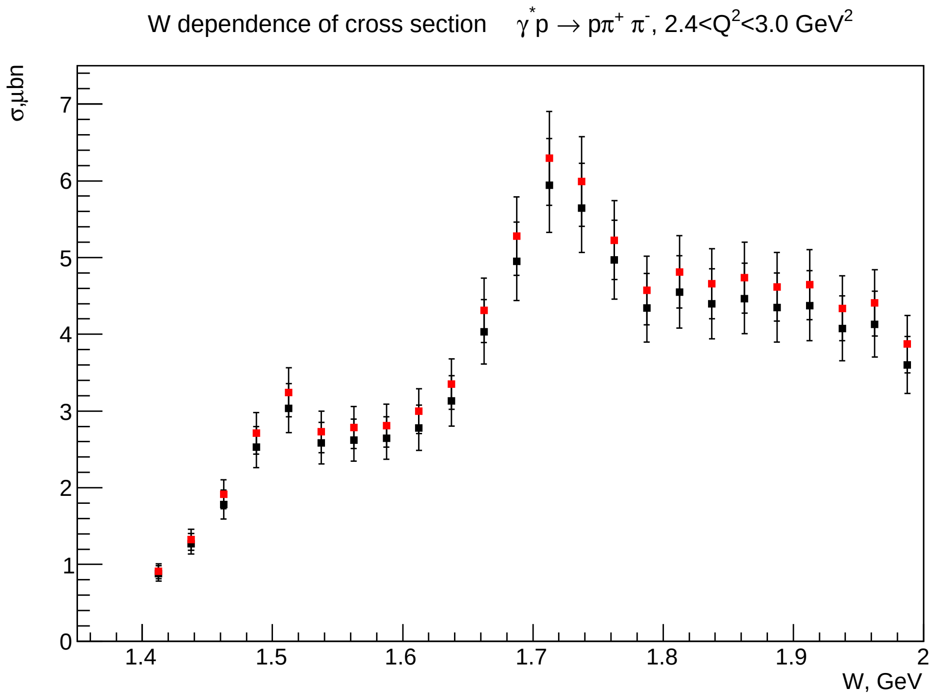

Figure 2.10: W dependence of cross section $\gamma^*p \to p\pi^+\pi^-$, $2.4 < Q^2 < 3.0$ GeV^2. Red - blind zones filled. Black - blind zones not filled

2.4 Overcoming edge effects in the $\pi^+\pi^-$ mass distribution

When evaluating the $\pi^+\pi^-$ invariant mass differential cross-sections we saw some unusual spikes at low values of invariant mass. In Fig. 2.11 we can see a large gap between the first and the second point forms an unphysical bump at $M_{\pi^+\pi^-}$ around 0.35 GeV. This may be a manifestation of significant edge effects. To study the behavior of mass distribution we decided to move the left and right boundaries and recalculated cross-sections in the new grid. The exact kinematic left boundary is $2M_\pi$, so to overcome edge effects we moved this boundary to the right. The corresponding right boundary is $W - M_p$ (which moves this boundary to the left). We kept on moving these boundaries until we reached saturation. For our particular example(Fig. 2.11) we shifted the left boundary to the right by 15 MeV and the right boundary to the left by 10 MeV. The result is shown in Fig. 2.12. There is substantial improvement, although the gap between the first and the second point as well as between the last and the second-to-last point is still too big. So we shifted the left boundary to the right by another 15 MeV and the right boundary to the left by another 10 MeV. The resulting distribution is in Fig. 2.13. No additional adjustment is needed. This procedure was done for every $W\&Q^2$ bin.

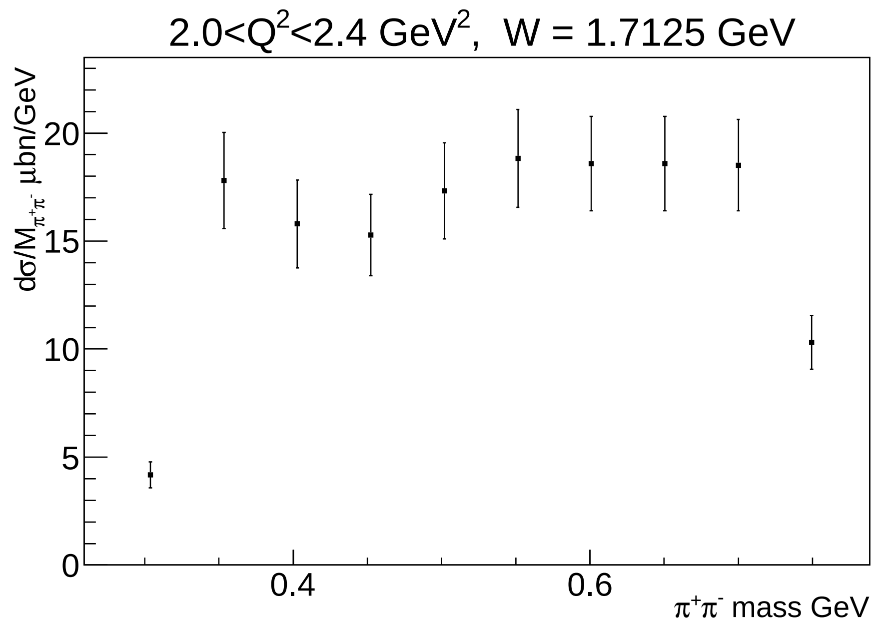

Figure 2.11: $\pi^+\pi^-$ invariant mass distribution evaluated in the range $[2M_\pi, W - M_p]$

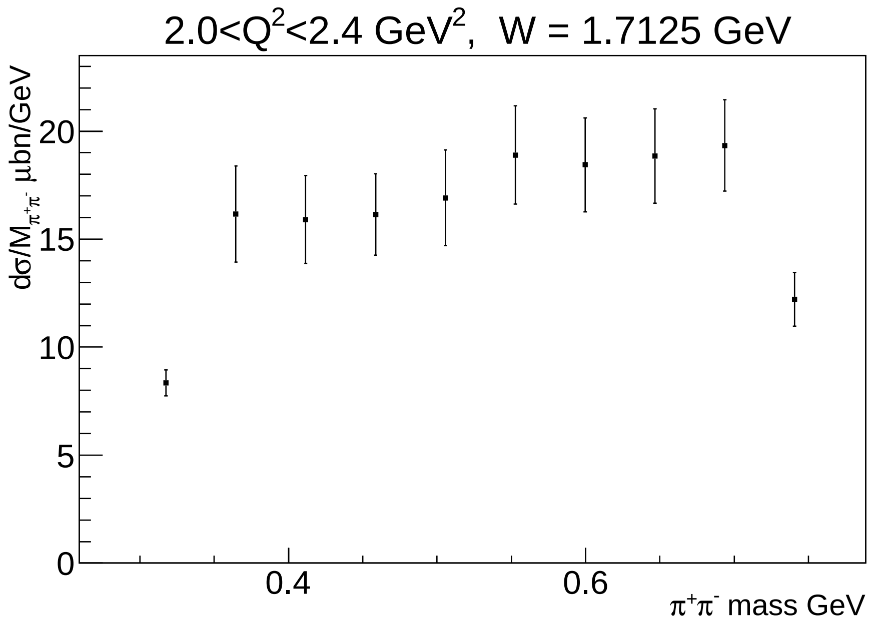

Figure 2.12: $\pi^+\pi^-$ invariant mass distribution evaluated in the range $[2M_\pi + 15\text{ MeV}, W - M_p - 10\text{ MeV}]$

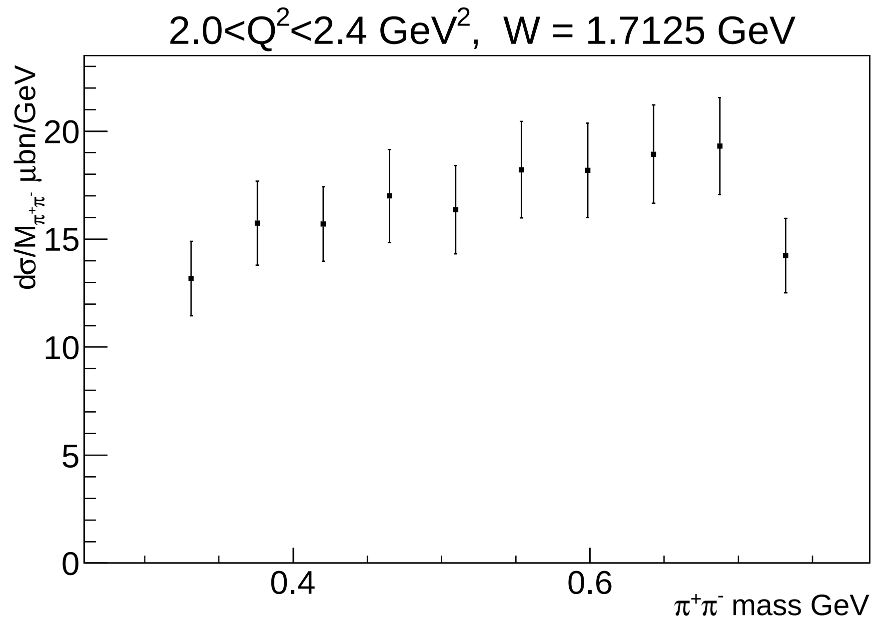

Figure 2.13: $\pi^+\pi^-$ invariant mass distribution evaluated in the range $[2M_\pi + 30\ \mathrm{MeV}, W - M_p - 20\ \mathrm{MeV}]$

Chapter 3

Radiative corrections

To estimate the influence of radiative correction effects, we simulated 2π events using the Genova event generator with included and excluded radiative effects. For the simulation of radiative effects in double pion electroproduction, the well known Mo and Tsai procedure[8] is used. In the Genova event generator the Mo and Tsai procedure is implemented assuming an "inclusive" hadronic tensor for the hard radiative part. We integrate the 5-fold 2π cross sections over 4 variables to get 1-fold differential cross-sections which we use in our physics analysis. This integration considerably reduces the influence of the final hadron kinematics variables on radiative correction factors for the analyzed single differential cross sections. So, the "inclusive" Mo and Tsai procedure looks more applicable to partially integrated 1-differential cross sections than in the case of non-integrated cross sections which we have for single pion data. The radiative correction factor R in (2.14) was determined as:

$$R = \frac{N^{2D}_{rad}}{N^{2D}_{norad}} \ , \tag{3.1}$$

where N^{2D}_{rad} and N^{2D}_{norad} are numbers of generated events in each (W, Q^2) bin with on/off radiative effects. In each (W, Q^2) bin covered by measurements we generated events with switched on/off radiative effects. Then we fit the inverse factor $1/R$ over the W range in each Q^2 bin. The inverse factor $1/R$ for the bin $4.2 < Q^2 < 5.0$ is plotted as function of W on Fig. 3.1. A few words should be said about the behavior of this factor. The radiation migrates events from the lower W to higher W and because the structure at W of around 1.7 GeV is the most prominent feature of the cross-sections(see Fig. 5.2) at high W, there is a small enhancing bump for the factor $1/R$.

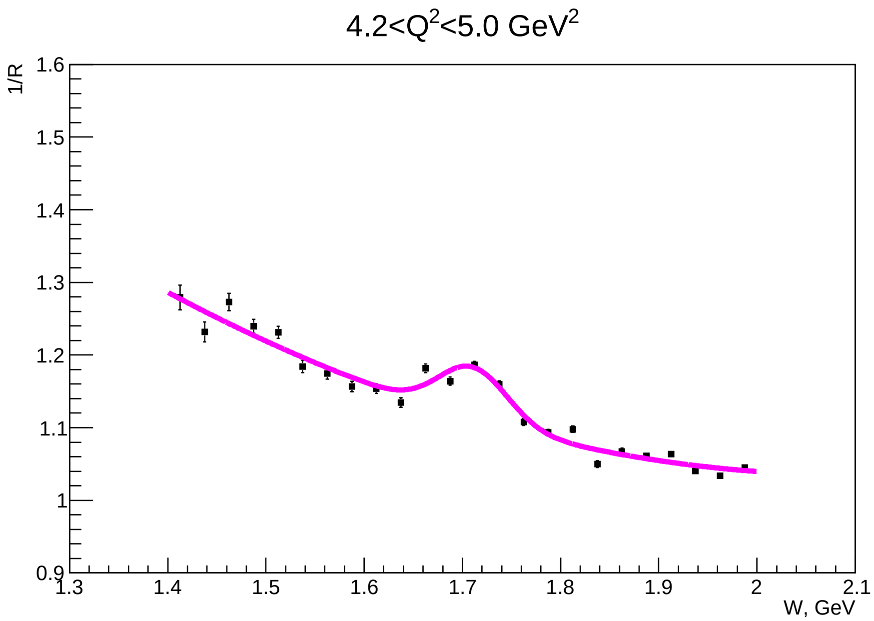

Figure 3.1: The radiative correction factor $1/R$ for $4.2 < Q^2 < 5.0$

Chapter 4

Systematic uncertainties

4.1 Uncertainties due to electron identification and normalization

One of the main source of systematic errors in this experiment is the uncertainty in the normalization. This can arise from miscalibrations of the Faraday cup, target density instabilities, and errors in determining the target length and its temperature, DAQ live-time and other factors. However, the presence of the elastic events in the data set allows us to check the normalization of the cross sections by comparing the elastic cross sections to the world data. This way we can combine the normalization, electron detection, electron tracking and electron identification errors into one global uncertainty factor. In Fig. 4.1 the ratio of the elastic cross section to the Bosted parametrization [10] is shown. The parametrization cross section are also "radiated", while the elastic cross sections from the CLAS data are not corrected for radiative effects. One can see most of the points are positioned within the red lines, indicating 10% offsets. This procedure allows us to assign 10% global error due to the normalization, target density fluctuations, Faraday cup uncertainty, electron identification and electron efficiency.

4.2 Uncertainties due to missing mass cut

We use a missing mass cut around the π^- peak to select two pion events. This cut causes loss of some events. Uncertainties due to such losses were estimated by using Monte Carlo simulations for the acceptance calculations. The error associated with the missing mass cut was estimated by calculating the difference in the cross sections with two different missing mass cut ap-

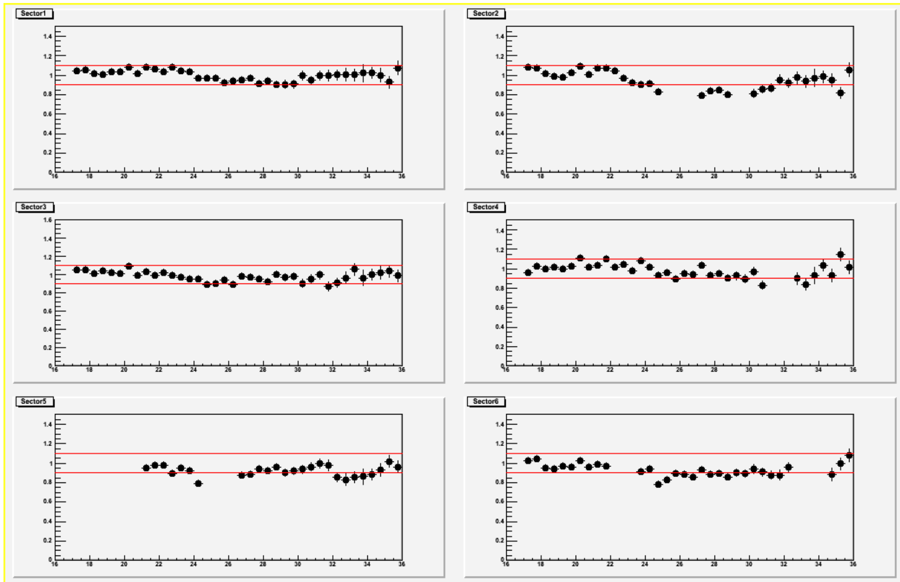

Figure 4.1: Ratio of elastic cross-section extracted from data and Bosted parametrization. Red lines correspond to 10% deviation.

plied both on the real data and Monte-Carlo data sample. The missing mass cut used in the analysis is $-0.04 < M^2_{\pi^- X} < 0.06$ GeV^2 so we used a different cut to estimate the systematic uncertainty due to the missing mass cut. This cut was more narrow than our cut namely: $-0.02 < M^2_{\pi^- X} < 0.03$ GeV^2.

We use the following method for estimating systematic uncertainties. In each case for a given observable(e.g. mass distribution) we can calculate the relative difference $(\sigma - \sigma_c)/\sigma$, where σ_c is the recalculated cross-section with the more narrow missing mass cut. We expect to see a gaussian-like distribution for the relative difference distribution. The difference between the center of this distribution and zero is a measure of systematic uncertainties. The errors due to the missing mass cuts are about 4.2% of the measured differential cross sections. The example of the relative difference for the $\pi^+\pi^-$ invariant mass distribution is shown on Fig. 4.2

4.3 Uncertainties due to hadron fiducial cuts

To estimate the influence of fiducial cuts to our results we recalculated cross-sections without applying fiducial cuts to hadrons. As described in the previous section we can construct the relative difference $(\sigma - \sigma_c)/\sigma$, where

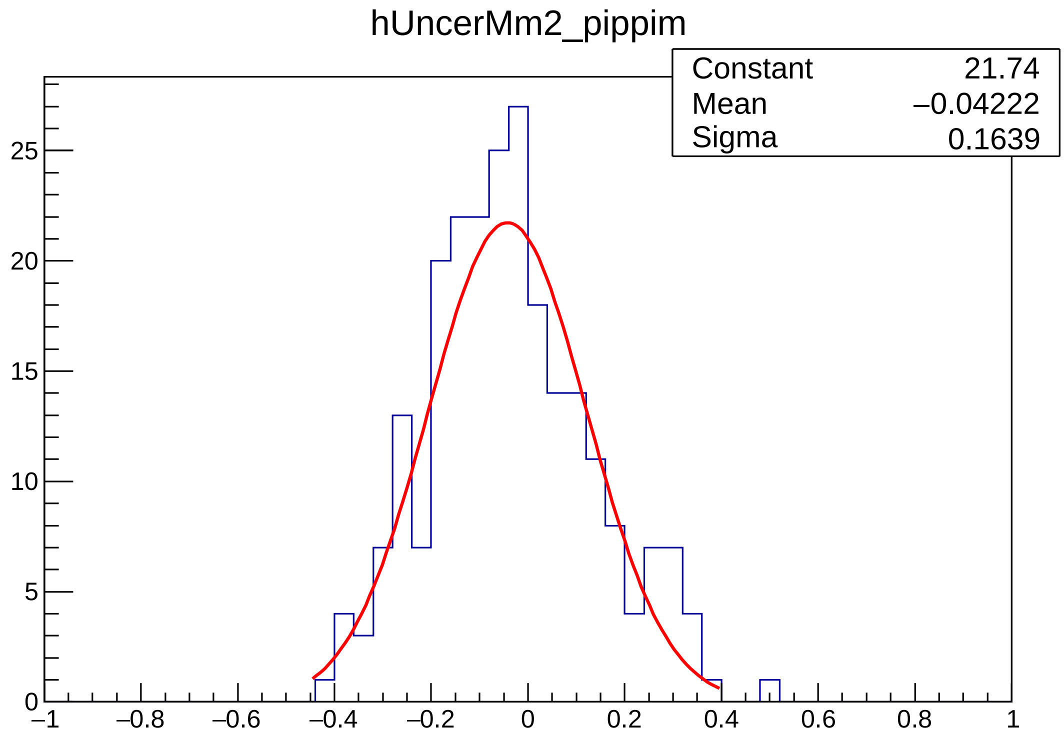

Figure 4.2: The relative difference $(\sigma - \sigma_c)/\sigma$ in $\pi^+\pi^-$ invariant mass distributions corresponding to different missing mass cuts.

σ_c - recalculated cross-section without hadron fiducial cuts. The result can be seen on Fig. 4.3. In this example we see systematic decrease(about 2%) of the cross-sections.

4.4 Uncertainties due to hadron identification cuts

We also varied the $\Delta\beta$ vs momentum cuts, which we use for hadron identification. In our analysis we apply 2σ cut, so to estimate the influence of these cuts to our results we recalculated cross-sections with 3σ cut. Again we construct the relative difference $(\sigma - \sigma_c)/\sigma$, where σ_c - recalculated cross-section with 3σ cut. The result can be seen on Fig. 4.4. In this example we see systematic increase(about 4.6%) of the cross-sections.

4.5 Summary

We estimated the main sources of the systematic uncertainties of extracted cross-sections. These include: electron identification and overall normalization($\sim$ 10%), missing mass cut($\sim$ 4.2%), hadron fiducial cuts($\sim$ 2%), hadron identification cuts($\sim$ 4.6%). Radiative effects were generated according to inclusive procedure[8]. The approximations used in this calculation may lead to systematic uncertainties of the order 5%[2]. We refer to the study of the sensitivity of the event generator performed for the case of ρ^0 production[11] to assign a systematic uncertainty of 5%. If we propagate quadratically all these sources we can obtain our overall systematic uncertainty of 14%

Table 4.1: Summary of sources of systematic uncertainties

Sources of systematics	uncertainty, %
Electron ID and normalization	10
Missing mass cut	4.2
Hadron fiducial cuts	2
Hadron ID cuts	4.6
Radiative corrections	5
Event Generator	5
Total	14

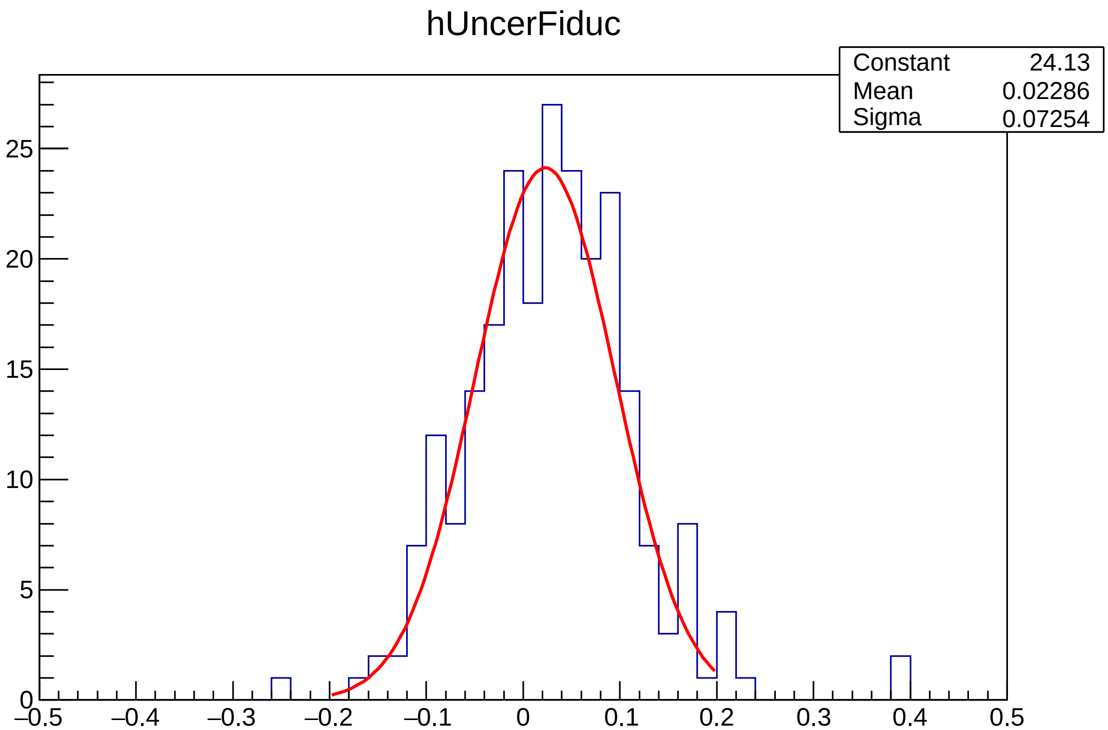

Figure 4.3: The relative difference $(\sigma - \sigma_c)/\sigma$ in $\pi^+\pi^-$ invariant mass distributions corresponding to enabling/disabling hadron fiducial cuts.

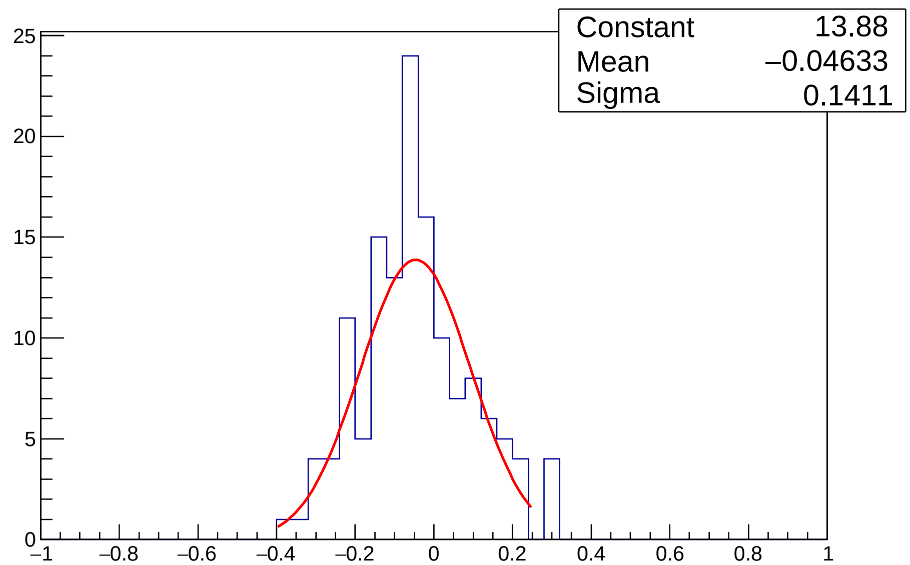

Figure 4.4: The relative difference $(\sigma - \sigma_c)/\sigma$ in ϕ of π^- distribution corresponding to different $\Delta\beta$ vs momentum cuts.

Chapter 5

Comparison with previous results

We can compare our results with previous published data. The most direct comparison is with the cross-sections extracted from the same run. We have a narrow overlap with other group whose aim is to study ρ^0 electroproduction. The comparison with these published cross-sections[12] is presented on the Fig. 5.1.

Also it is useful to compare with previously published[13] cross-sections of double pion production with detailed W-dependance. Because of the different Q^2 it is convenient to present Fig. 5.2 in a logarithmic scale. Although we should note that the comparison is more difficult in that case because the virtual photon cross-section depends on the beam energy.

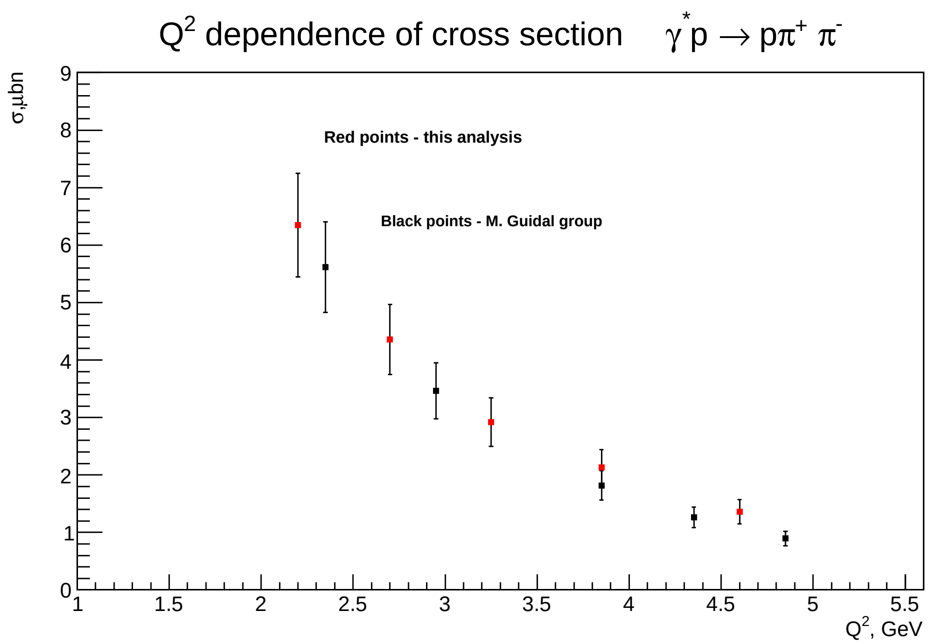

Figure 5.1: Q^2 dependence of cross section $\gamma^* p \rightarrow p\pi^+\pi^-$, $W = 1.99$ GeV.

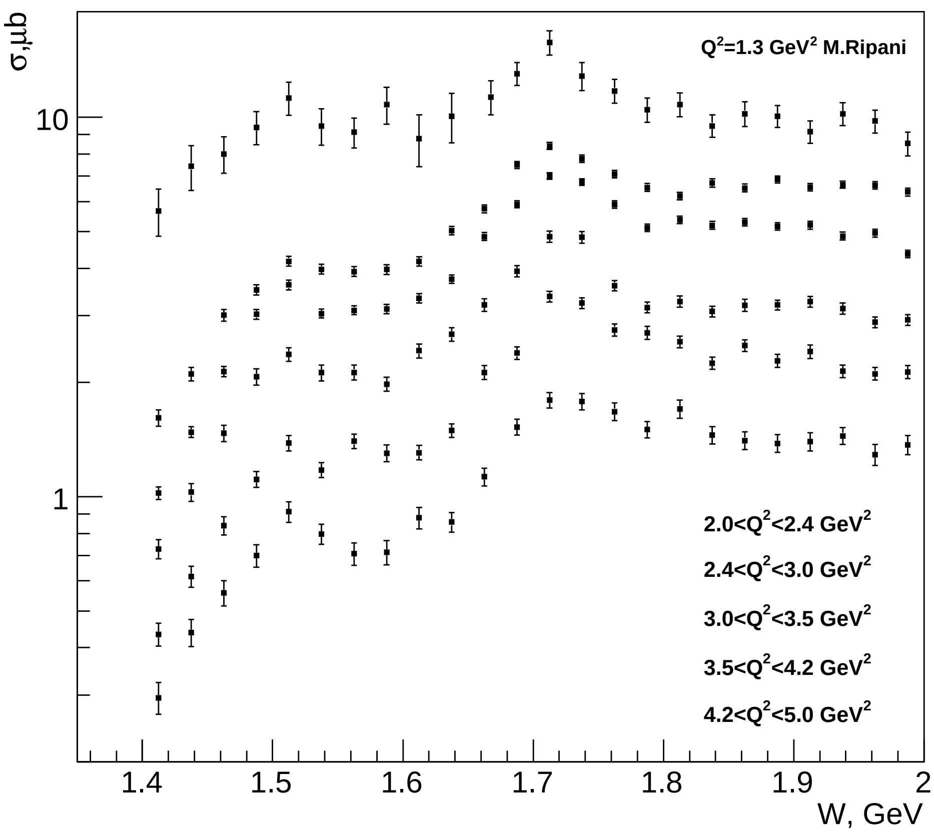

Figure 5.2: W dependence of cross section $\gamma^* p \to p\pi^+\pi^-$ for various Q^2.

Bibliography

[1] K. Egian, CLAS-NOTE 99-007, (1999).

[2] L.Morand, Deeply virtual production of the ω meson CLAS NOTE(2006)

[3] M. Osipenko, A. Vlassov and M. Taiuti CLAS NOTE 2004-020(2004)

[4] Kijun Park Electron Asymmetry in the in the Mass region of the and higher resonances(2004)

[5] Kijun Park CLAS NOTE 2003-012(2003)

[6] D.Dore, Selection des pions et des proton, Note interne Saclay (2002)

[7] S.A. Morrow, Proton Energy Loss Correction for e1-6a, Note interne de e1-6(2003)

[8] L.W. Mo, Y.S. Tsai, Radiative Corrections to Elastic and Inelastic ep and μp Scattering, Rev. Mod. Phys. **41**, 205 (1969)

[9] V.I. Mokeev, V.D. Burkert, T-S.H. Lee et al. Phys.Rev. **C80** 045212, (2009)

[10] P. E. Bosted, Empirical fit to the nucleon electromagnetic form factors, Phys. Rev. **C51**, 409, (1995).

[11] C. Hadjidakis, Electroproduction de meson ρ virtualit intermediare. These de doctorat, Univerite Paris(2002)

[12] S.A. Morrow et al. Exclusive ρ^0 electroproduction on the proton at CLAS, Eur. Phys. J. A **39**, 5-31(2009)

[13] M. Ripani, et al. Phys. Rev. Lett. **91**, 022002

[14] G.V. Fedotov et al. Phys.Rev. **C79**, 015204(2009)

[15] M.Osipenko et al. Phys.Rev. **C73**, 045205(2006)